BBA - General Subjects 1869 (2025) 130818

Contents lists available at ScienceDirect

BBA - General Subjects

journal homepage: www.elsevier.com/locate/bbagen

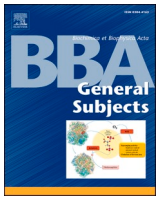

Review

There is more to scanning than meets the eye: Raster Image Correlation Spectroscopy

Irene Gialdini [a], Jelle Hendrix [b,*], Don C. Lamb [a,*]

[a] Department Chemie and Center for NanoScience, Ludwig-Maximilians-Universität München, Munich, Germany
[b] Dynamic Bioimaging Lab, Advanced Optical Microscopy Centre and Biomedical Research Institute, Hasselt University, Agoralaan C (BIOMED), Hasselt, Belgium

ARTICLE INFO

Keywords:
Raster Image Correlation Spectroscopy (RICS)
Cross-correlation RICS (ccRICS)
Fluorescence fluctuation imaging
Confocal imaging
Live-cell imaging
Molecular diffusion
Molecular interactions

ABSTRACT

Raster Image Correlation Spectroscopy (RICS) is a confocal image analysis method that can measure the diffusion and interactions of fluorescently labeled molecules in real time in solution and in living cells. RICS is easy to implement on commercial confocal microscopes and allows detailed investigations of complex biological systems and pathways. The method is especially robust for measurements in living cells using commonly used labels such as fluorescent proteins. Moreover, since its invention in 2005, the robustness and applicability of RICS has been significantly increased to allow, e.g., straightforward kinetic analyses, advanced image segmentation, parameter mapping, and multi-species analysis. In this review, we describe the methodological principles of RICS in a manner that is accessible to a broad readership, position RICS in relation to other fluorescence fluctuation techniques, highlight recent methodological advances and present exemplary applications of the method. With this review, we hope to facilitate the implementation of this powerful method into the everyday repertoire of confocal imaging approaches.

1. Introduction

The characterization of complex biological systems relies on understanding the orchestrated movements of the molecules involved. The mobility of a molecule in its environment, either in solution or in living cells, is tightly associated with its size and with the viscosity of the environment. An alteration in the molecular size, caused for instance by binding with an interaction partner, as well as a change in viscosity, for example due to motion into condensates, will affect its diffusion. This makes molecular diffusion a straightforward read-out for many biological processes such as oligomerization, degradation or transport, and can be used to quantify interaction affinities, complex stoichiometries and medium viscosity. Nowadays, thanks to the advances in fluorescence microscopy and the availability of good fluorescent labels, precise diffusion measurements can be done *in vitro* and *in vivo* by means of fluorescence fluctuation spectroscopy (FFS).

FFS comprises a family of fluorescence analysis techniques that quantify the mobility, size, concentration and/or (homo- or heteromeric) interaction of fluorescently labeled (bio-)molecules. FFS methods infer molecular properties from a statistical correlation analysis of the fluorescence intensity fluctuations and can be performed in a confocal setting (as in, e.g., a confocal microscope) as well as a wide-field setting (as in, e.g., a TIRF microscope). Anything that leads to non-stochastic fluctuations in fluorescence intensity, such as a burst of photons due to the transit of a molecule through the observation volume, will correlate. Although translational diffusion is often the main parameter investigated when carrying out FFS methods, fluorescence intensities can also fluctuate because of other processes, depending on the properties of the sample (and the employed microscope). Such processes that lead to changes in fluorescence intensity, for instance, rotational diffusion, molecular interactions and/or fluorophore blinking, will correlate. The first implementation of FFS was Fluorescence Correlation Spectroscopy (FCS), which was developed in 1972 [1] and originally used to quantify molecular diffusion, molar concentration and interactions [2,3]. The applicability of FCS was greatly enhanced, especially for the biological community, by combining it with confocal microscopy [4]. In FCS, the temporal duration of the fluorescence fluctuations is analyzed by computing an autocorrelation function (ACF), which evaluates the self-similarity of the intensity trace as a function of time. Intuitively, the slower the diffusion of molecules, the longer the self-similarity of the resulting traces. FCS is a powerful tool for studying the properties of diffusing molecules over a broad range of time scales, from seconds

* Corresponding authors.
E-mail addresses: jelle.hendrix@uhasselt.be (J. Hendrix), d.lamb@lmu.de (D.C. Lamb).

https://doi.org/10.1016/j.bbagen.2025.130818
Received 28 November 2024; Received in revised form 5 May 2025; Accepted 9 May 2025
Available online 10 May 2025

down to microseconds and, in some implementations, even picoseconds [5]. However, classic FCS only observes molecules in a stationary ~femtolitre sized volume within the sample. The contextual information (i.e. image) in the vicinity of the measurement is not available. Such info is indeed irrelevant if the sample is a homogeneous solution in which the particles of interest move about isotropically. However, for more complex biological systems such as living cells, the diffusion properties of particles may depend on their location, arguing the need for imaging-based FCS methods. In addition, as classic FCS focuses the laser light into a defined location for one or even a few minutes, this can lead to local dye photobleaching and eventually to phototoxicity when living biological systems are studied. [6]

The first approach to incorporate local spatial information with fluctuation spectroscopy was scanning FCS (sFCS), in which the focus of the laser beam is rapidly moved across the sample by either translating the sample stage [6,7] or scanning the laser beam [8,9]. The focus can be scanned in circular orbits [10] or following a linear trajectory [11], maintaining a high temporal resolution while adding a spatial component to the FCS analysis. Additionally, sFCS is advantageous when dealing with diluted samples or slowly diffusing molecules. With classical FCS, very long acquisition times are required to compensate for the infrequent appearance of the fluorophore in the confocal spot. With sFCS however, multiple spots are sampled in rapid succession, increasing the probability of detecting a particle. As such, sFCS has been extensively employed to investigate molecular aggregation and slow dynamics at the cell membrane [9,11–14].

To further extend the area of analyses beyond a single line (or orbit), Image Correlation Spectroscopy (ICS) was developed in 1993 [15]. By performing correlation analysis on a confocal image, possibly containing an entire cell, ICS can provide a simultaneous overview of spatial heterogeneities. Originally, ICS used images of fixed fluorescent samples obtained by confocal laser-scanning microscopy as input, rather than the fluorescence time traces used in FCS. In ICS, the fluorescence fluctuations come from the spatial distribution of objects in the fluorescence image and the correlations are calculated between pixels in the image rather than between points in time. By capitalizing on the fact that correlation experiments are assumed to be ergodic, the molecular parameters determined from a single location over time should be identical to the ones obtained by imaging over a larger region of space at one point in time. To improve the signal-to-noise ratio of the spatial ACF (SACF), it is then averaged over many images. This type of spatial correlation allows one to obtain information on the molecular concentration and aggregation state of molecules in a sample, but not on their diffusion properties. To include the temporal information, Wiseman and colleagues, around the turn of the century, developed a variant of ICS called Temporal ICS (TICS) [16], in which the fluorescence fluctuations are correlated in time (rather than in space), through an entire image stack. In other words, instead of correlating neighboring pixels of a single image, as is done in ICS, TICS analyzes the fluctuations in the same pixel or group of pixels i,j across an image stack. Since the correlation occurs between frames, however, the investigated molecules need to be slow enough to be captured across consecutive frames, which, in standard confocal microscopy, are acquired on the order ~1 frame per second. Although this typically matches well with the diffusion rates of, e.g., membrane proteins [16], the diffusion rates of biomolecules in other cellular locations such as the cytoplasm are too fast to be captured by TICS.

To bridge the gap between the high temporal resolution of single-point FCS on the one hand, and the spatial component offered by ICS, Digman and colleagues introduced Raster Image Correlation Spectroscopy (RICS) in 2005 [17]. RICS is based on the realization that, if confocal laser-scanning microscopy is performed on samples containing diffusing molecules, and if the scan speed is set appropriately, the diffusion properties of molecular are encoded in the resulting pixel fluorescence intensity fluctuations. Identical to ICS, the correlation is performed between pixels in the same frame along the x and y axis of the image. Similar to FCS, RICS allows one to obtain dynamic information in the microsecond to second time scale [17,18], opening the possibility of investigating biological processes not only in membranes but also in other compartments of living cells.

In this review, we will illustrate the basic principle of RICS and its further developments, which enable us to improve the spatial resolution of RICS and obtain detailed diffusion maps (Arbitrary RICS, Local RICS, STED-RICS), as well as to perform robust multicolor analyses (dual-color RICS) with minimal to no contribution from crosstalk (PIE-RICS, Spectral RICS and lifetime filtered RICS). RICS and its developments open the possibility of investigating several molecular processes including, but not limited to, binding and unbinding [19–21], protein homo- and hetero-dimerization, oligomerization or aggregation [22–26], DNA degradation [27], and interactions with cellular components such as chromatin or membranes [28–30]. RICS allows one to characterize the molecular architecture of diverse biological systems *in vitro*, in living cells and even *in vivo*, quantifying their stoichiometry, interaction affinities, local concentration, and monitoring their behavior in a time and space dependent manner. All of this quantitative information is available for extraction from a simple confocal raster scanned image.

2. Principle and experimental guidelines for RICS

In 2005, Digman and collaborators developed Raster Image Correlation Spectroscopy, which decreases the disparity in time resolution between single-point FCS (microsecond scale) and ICS (seconds) techniques [17]. RICS uses an ICS analysis to extract the inherent time information captured in a raster-scanned image (Fig. 1A-C), the default imaging approach of a confocal laser-scanning microscope. With raster-scanning, the time information is determined by the scanning motion itself, which follows a sawtooth pattern. The laser beam is rapidly moved across the x axis according to the pre-set pixel dwell time τ_p (microseconds). At the end of the first line, the beam is retracted to the initial x position and simultaneously shifted down by one pixel in the y direction, where a second line scan is started (Fig. 1A). When molecules are diffusing on the time scale of the scanning, dynamic information can be extracted using RICS.

Due to the time necessary for scanning a single line in x, the acquisition in the y direction is significantly slower and is governed by the line time τ_l (milliseconds), i.e. the time difference between the start of consecutive line scans. For a linear scanner, the time relation between pixels is well defined throughout the image. The different scanning speed along the two axes enables one to probe dynamics over timescales from μs to s. A fast-diffusing molecule will be mainly detected in a few adjacent pixels along the x axis because, upon scanning of the next line, the molecule will have diffused away. However, due to the fast diffusion, there is a possibility of finding the molecule further away. In contrast, slower molecules will be in a very similar location as the laser scan returns for the next line (Fig. 1D). These different behaviors become visible in the SACF. To calculate the SACF, a copy of the obtained image is made and shifted in the x and y dimensions by spatial lags defined as ξ and ψ, respectively. The original image is then multiplied pixelwise by the shifted image and the average value calculated. The process is repeated for each ξ and ψ combination (Fig. 1B, C). This is the same procedure that was used in the initial ICS analysis. Hence, the analysis is typical referred to in the field as a spatial ACF. However, it is important to note that, in a RICS experiment, the correlation is calculated between pixels that are recorded at different times. It is this 'hidden' time information that makes RICS so powerful. Hence, the SACF in RICS includes a spatial and temporal component. However, to be consistent with literature, we will retain the terminology of spatial ACF in this review.

Many frames are acquired to improve the accuracy of the analysis: the correlation is performed in each frame individually, and then the average of all SACFs over the movie is computed. The SACF of fast-diffusing molecules will exhibit a fast-decaying, narrow autocorrela-

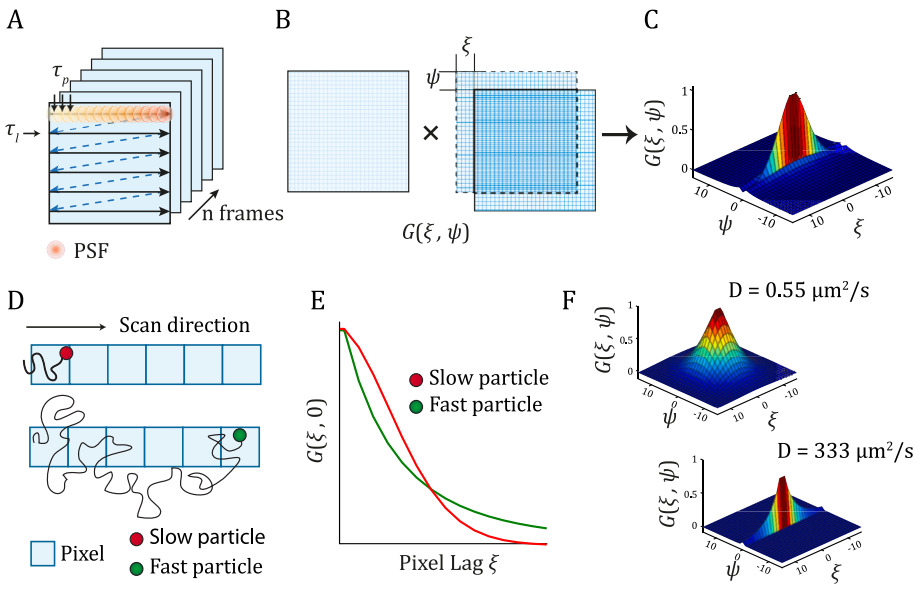

Fig. 1. Principle of RICS. A) Illustration of data collection for a typical RICS experiment in which each frame is acquired by raster scanning with a pixel dwell time τ_p and a line time τ_l. B) Calculation of the spatial correlation. The acquired image is copied and shifted by a pixel lag (ξ, ψ) and the correlation between the original image and the shifted copy is calculated. This process is repeated for every (ξ, ψ) combination of interest. The correlation is computed for each frame individually and then averaged, resulting in C) the 2D spatial autocorrelation function (SACF). The depicted SACF represents the mCherry fluorescent protein expressed in HeLa cells, transfected 18 h before imaging with X-tremeGENE™ 9 DNA (Roche). The data were acquired at 37 °C on a raster scanning confocal microscope as described in [23] with a pixel dwell time of 11 µs, and analyzed with the MATLAB based software PAM (MIA submodule) [31]. The fit diffusion coefficient is 30 µm^2/s. D) During image acquisition, a slow diffusing particle (red) will be observed across very few pixels. Within the same time interval, a fast-diffusing particle (green) can be observed across many pixels but might also rapidly move outside of the volume of illumination. As a result, the correlation relative to the fast particle (green curve) will have an initial rapid decay, as shown by E) the 1D SACF slices. However, the fast particle has a probability of being observed in pixels further away, and thus the correlation will not immediately decay to zero, in contrast to the correlation of the slow particle. F) The 2D SACFs obtained by performing RICS analyses for different diffusion rates. The slow diffusion (D = 0.55 µm^2/s) SACF was determined from cytosolic measurements of the HIV-1 Gag protein fused with mCherry and expressed in HeLa cells, while the fast diffusion SACF (D = 333 µm^2/s) is given by ATTO565 freely diffusing in dPBS. (For interpretation of the references to color in this figure legend, the reader is referred to the web version of this article.)

tion function along the x axis with a non-zero probability at longer times whereas that of slowly diffusing molecules will also display a broader and more circular SACF (Fig. 1D-F).

Before continuing with our discussion of RICS, we first briefly explain the temporal autocorrelation function (ACF) for single-point FCS [1,18]. FCS typically measures the diffusion of molecules in and out of the point-spread function (PSF) of the measurement system. The PSF describes the detected 3D diffraction pattern from light emitted by a point-like object, such as a fluorophore, present in the excitation volume. For single photon excitation and confocal detection, the PSF is characterized by an ellipsoidal shape that can be modeled with a 3D Gaussian function. The normalized ACF (i.e. the ACF normalized to the square of the average intensity) is given by:

$$G(\tau) = \frac{\langle \delta I(t) \delta I(t+\tau) \rangle_t}{\langle I(t) \rangle_t^2} \tag{1}$$

where the triangular brackets indicate the average value, in this case a time average, $I(t)$ is the fluorescence intensity as a function of time, $\delta I(t) = I(t) - \langle I(t) \rangle_t$ represents the fluctuation of fluorescence intensity with respect to the average value and τ is the lag or delay time. The ACF evaluates the self-similarity of the fluorescence trace as a function of the delay time τ. If we assume a 3D Gaussian volume of observation that is much smaller than the extent of the sample, the ACF can be analytically solved and is given by:

$$G(\tau) = \frac{\gamma}{N}\left(1 + \frac{4D\tau}{\omega_r^2}\right)^{-1}\left(1 + \frac{4D\tau}{\omega_z^2}\right)^{-\frac{1}{2}} \tag{2}$$

where D is the diffusion coefficient of the molecule, and ω_r and ω_z represent the radial and axial distance from the center of the observation volume (i.e. product of the excitation and detection PSFs) to where the fluorescence intensity has decreased by a factor of $1/e^2$. (Technically speaking, ω_r and ω_z refer to the observation volume, but are equivalent to the fluorescence intensity profile in the regime where the fluorescence response is linear). γ is a geometrical factor to correct for the shape of the observation volume. For confocal illumination, in which the geometry of the observation volume can be approximated to a 3D Gaussian shape, γ is equal to $2^{-3/2} = 0.35355$. The effective observation volume is then equal to [32,33]:

$$V_{eff} = \left(\frac{\pi}{2}\right)^{3/2} \omega_r^2 \omega_z \tag{3}$$

For two-photon excitation, the diffusion term $4D$ should be replaced with $8D$ and the observation volume can be approximated with a 2D Gaussian-Lorentzian, with a γ factor equal to 0.185 [32]. N is the average number of particles in the observation volume and can be utilized to calculate the molecular concentration (C) according to:

$$N = C N_A V_{eff} \tag{4}$$

$$C = \frac{N}{N_A V_{eff}} \tag{5}$$

with N_A being the Avogadro's number.

In RICS, the spatial autocorrelation function evaluates the self-similarity of an experimental image with a copy of it, shifted as a function of different spatial lags in x and y (ξ and ψ, respectively, Fig. 1B).

$$G_S(\xi, \psi) = \frac{\langle \delta I(x,y) \delta I(x+\xi, y+\psi) \rangle_{x,y}}{\langle I(x,y) \rangle_{x,y}^2} \tag{6}$$

here, $I(x,y)$ is the fluorescence intensity at each pixel, $\delta I(x,y)$ is the fluorescence intensity fluctuations with respect to the average I of the entire frame, and the brackets, in this case, indicate the spatial average over mutual pixels within the products of the images. The spatial autocorrelation function in RICS is the imaging equivalent of the temporal autocorrelation in FCS.

Interestingly, since the data are acquired using raster-scanning with a constant scanning speed and linear spacing between adjacent lines, there is a well-defined relationship between the position of the pixel in the image and the time it was measured. With raster scanning, the time relation between any pair of pixels, spaced by the same pixel lags (ξ,ψ), is also the same. This means that the spatial autocorrelation $G(\xi,\psi)$ can be sampled anywhere in the image, similarly to $G(\tau)$ in FCS, which can be calculated anywhere along the time trace. In fact, the spatial lags ξ and ψ can be converted to an absolute delay time as follows:

$$\tau_\xi = \xi \times \tau_p \tag{7}$$

$$\tau_\psi = \psi \times \tau_l \tag{8}$$

where τ_p and τ_l are the pixel time and line time. The total delay time τ_{total} between two pairs of pixels spaced ξ and ψ is equal to:

$$\tau_{total} = \tau_\xi + \tau_\psi \tag{9}$$

and corresponds to the same time delay τ used in a typical FCS analysis.

Using the total delay time, we can plot data collected in a RICS experiment as a 1D correlation function similar to FCS (Fig. 2). In this way, it becomes clear that, with both techniques, it is possible to investigate diffusion dynamics over relatively similar timescales from µs to s. For a fast-diffusing molecule (Fig. 2A), the form of the RICS ACF approaches that of FCS. The time scale of this correlation (10^{-5}–10^{-3} s) is in the range or faster than the RICS line time τ_l, indicating that the decay is observable in only ξ axes of the SACF. This is another way of demonstrating that the diffusion of fast species is nicely captured by the line scanning in the x direction. For slow diffusing molecules (Fig. 2B-C), an oscillating pattern appears in the ms regime. This is due to the raster scan pattern: once the first line is acquired, the laser is retracted, and a second line is scanned where y has been shifted down by 1 pixel. Due to the shift in y, the correlation function is spatially shifted from the original position and the peak amplitude decreases accordingly. Each oscillation corresponds to a new line scan and enables quantification of slower dynamics along the y axis. In both cases, the RICS correlation nicely approaches the FCS one, but there is never an overlap, because the origin of each scanned line is shifted.

As stated in the introduction, fluctuations in fluorescence intensity can also be due to other processes such as conformational changes measured via FRET- or photoisomerization-related fluorescence enhancement (PIFE) [34,35] or molecular tumbling. However, in this review, we will concentrate on intensity fluctuations due to translational diffusion.

In this case, the spatial correlation function $G_S(\xi,\psi)$ is composed of two terms:

$$G_S(\xi,\psi) = S(\xi,\psi) \times G_D(\xi,\psi) \tag{10}$$

where $G_D(\xi,\psi)$ is the temporal term that is determined solely by molecular diffusion and is identical to the FCS diffusion term, and a spatiotemporal term, also commonly referred to as the scanning term ($S(\xi,\psi)$), which arises due to the raster-scanning being performed while molecular diffusion occurs [17]. The terms are given by:

$$S(\xi\psi) = exp\left(-\frac{\left[\left(\frac{\xi\delta x}{\omega_r}\right)^2 + \left(\frac{\psi\delta y}{\omega_r}\right)^2\right]}{\left(1+\frac{4D\left(\left|\tau_p\xi+\tau_l\psi\right|\right)}{\omega_r^2}\right)}\right) \tag{11}$$

$$G_D(\xi\psi) = \frac{\gamma}{N}\left(1+\frac{4D\left(\left|\tau_p\xi+\tau_l\psi\right|\right)}{\omega_r^2}\right)^{-1}\left(1+\frac{4D\left(\left|\tau_p\xi+\tau_l\psi\right|\right)}{\omega_z^2}\right)^{-1/2} \tag{12}$$

where the pixel dimensions are denoted as δx and δy, and $\|$ indicates the absolute value.

Since its development, RICS has been widely used to unravel various aspects of cell biology. Recently, for example, Pannek et al. investigated the recycling route of albumin in mouse macrophages mediated by FcRn, a major histocompatibility complex (MHC) class-I like molecule that is known to be involved in rescuing albumin from lysosomal degradation [36]. Macrophage cells were incubated with albumin and, after albumin's internalization into endosomes, its diffusion was monitored by RICS (Fig. 3). The results revealed that albumin is present as two species: a freely diffusing species (D = 51 ± 7 µm^2/s), which accounts for 45 % of the total signal, and a slowly diffusing component (D = 0.07 ± 0.02 µm^2/s), which is subjected to transient immobilization due to binding with FcRn. This finding was confirmed by incubating the cells with a non-FcRn binding mutant of albumin. In this case, the slowly diffusing fraction was significantly reduced. This result confirmed that FcRn plays a role in the recycling of internalized albumin, pointing towards a direct interaction between the two proteins.

2.1. Choosing the right experimental settings

The performance of RICS is affected by several experimental parameters such as, but not limited to, the scan speed, the pixel size, the number of frames, the size of the region of interest (ROI) and the brightness of the molecule of interest. All these parameters contribute to the signal-to-noise ratio (SNR) and it is therefore important to choose them properly to ensure good data quality. A SNR greater than 10 means that the amplitude of the correlation function is over 10 times larger than the noise of the correlation function itself, which is usually enough

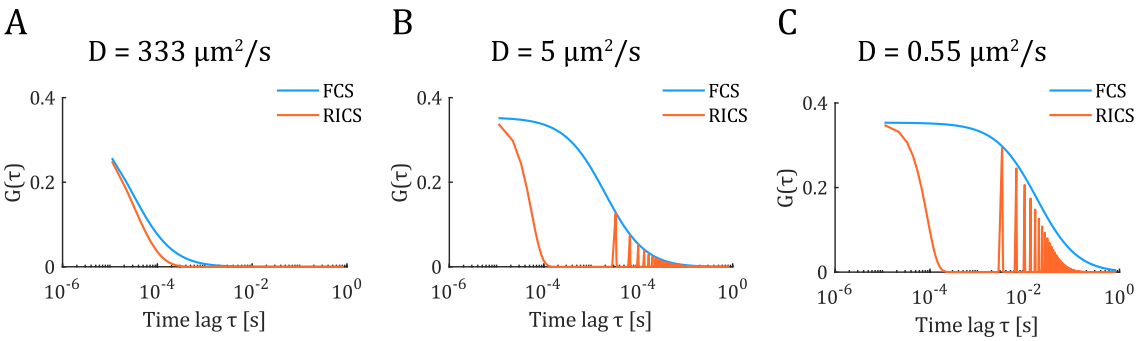

Fig. 2. Comparison between FCS and RICS analyses in one dimension. Calculated FCS and RICS curves for diffusive species with A) D = 333 µm^2/s, B) D = 5 µm^2/s and C) D = 0.55 µm^2/s. The pixel dwell time was set to 11 µs, the line time to 3.3 ms and the pixel size to 40 nm in order to achieve optimal oversampling of the PSF (see Section 2 for details).

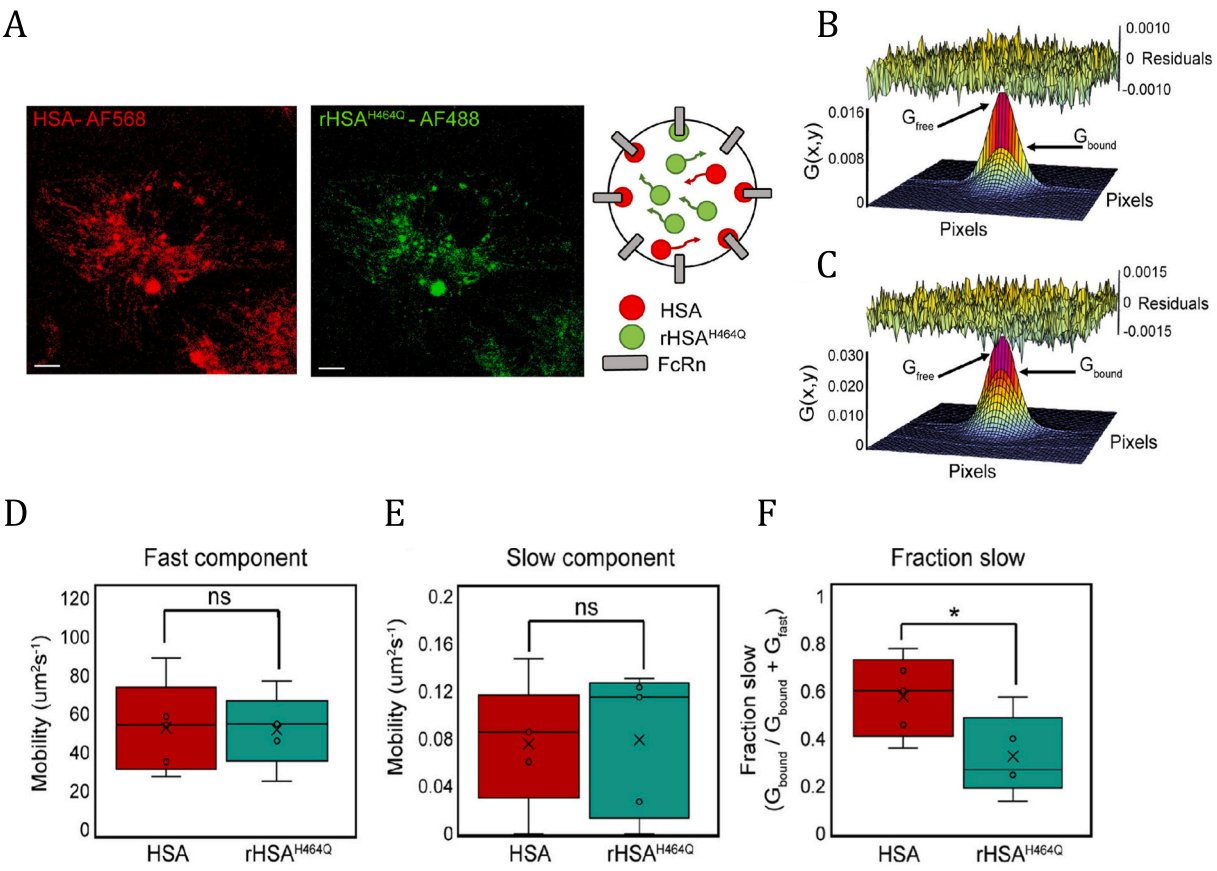

Fig. 3. RICS analyses of uptake in endocytic vesicles of wildtype human serum albumin (HSA) and rHSA^{H464Q}, an HSA mutant not capable of binding FcRn. Reproduced from Figure 9 of [36] under the terms of the Creative Common Attribution-Noncommercial-Share Alike 4.0 Int. (CC-BY-NC-SA 4.0) License (https://creativecommons.org/licenses/by-nc-sa/4.0). A). Confocal images of bone marrow-derived macrophages treated with a colony stimulating factor and incubated with labeled Alexa Fluor 565 (HSA-AF565) and rHSA^{H464Q} labeled with AF488 (rHSA^{H464Q}-AF488). The scale bar is 5 μm. On the right, a schematic of how the different HSAs interact with FcRn inside a vesicle. B, C) 2D-ACFs obtained from RICS analyses of HSA-AF565 (B) and rHSA^{H464Q}-AF488 (C). The amplitude of the free diffusing component is indicated as G_{free}, while the bound component is indicated by G_{bound}. D, E). Diffusion coefficient of the fast, freely diffusing component (D) and the slow, bound component (E) of HSA-AF565 and rHSA^{H464Q}-AF488. F). Fraction of HSA-AF565 and rHSA^{H464Q}-AF488 that exhibit slow mobility, attributed to be FcRn bound. For panels D-F, $N = 5$ cells and the box and whisker plots show the minimum, maximum, sample median, and first and third quartiles. The means are shown by a cross. The data were analyzed by unpaired two-tailed Student's *t*-test. *$p < 0.05$.

to obtain reliable data with well-defined confidence intervals. The SNR can be estimated as the ratio of the *maximum amplitude* of the correlation function to the average of the *standard deviation* of the data points, the latter of which can be approximated from the $\psi = 0$ row of the SACF. A detailed analysis of the contribution of each RICS settings to the accuracy and precision of obtained parameters has been performed by Longfils and colleagues [37], which also provide guidelines for their optimization.

2.1.1. Scan speed

For optimal RICS measurements, it is important to match the scan settings with the diffusion constant of the molecule of interest, when possible. When the molecule moves faster than the scanning of the focus in the *x* axis (i.e., scan speed too slow), it will not have time to contribute to the correlation function, which will decay very rapidly. On the contrary, if a molecule is moving slower than the laser scan speed (i.e. scan speed too fast), it will appear as immobile particle (on the time scale it takes to scan over the object) and the ACF will have the shape of the PSF (technically, the square of the PSF), as shown in figure 1 of the publication by Brown et al. [38]. As a rule of thumb, the maximum value for the pixel dwell time is defined as [39]:

$$\tau_p = \frac{\omega_r^2}{4D} \tag{13}$$

A more precise and analytical calculation of the most suitable pixel dwell time as a function of D was performed by Longfils et al. [37]. Typically, the pixel dwell time should be between 8 and 20 μs. For very fast diffusing molecules ($D > 100$ μm^2/s), a pixel dwell time of 5 μs is recommended. For $D \sim 10$ μm^2/s, a τ_p of 5–20 μs is sufficient. For molecules with a diffusion coefficient around $D \sim 0.1$ μm^2/s, the line time becomes more important and should be 12–58 ms [37]. While one can continue to optimize the scanning speed for even slower motions, it becomes preferable to apply other ICS methods. Additionally, when measuring in living cells, the optimal scan time cannot always be applied due to cell and cell organelle motions. As we will discuss more in detail in the detrending section of this review (Section 2.2), cellular movement, subcellular motion or drift can be corrected for and removed from the image stack, provided that they are quasi static during the recording of a few frames. This, in turn, may require having to image faster than would be ideal for the diffusion rate of the molecule of interest.

2.1.2. Pixel size

Another important requirement for accurate RICS experiments is having enough data points on the spatial scale of the PSF. It is the deviation of the SACF from the shape of the PSF (technically, the square of the PSF) that contains the dynamic information in the measurement. Hence, there should be a minimum of ~10 data points within the spatiotemporal decay of the ACF for robust data fitting. This is achieved in practice by having a pixel size at least 4 times smaller than the PSF,

typically ≤50 nm [37–39].

2.1.3. Number of frames

Although the SACF is calculated on a single image, several frames are typically acquired and averaged to improve the accuracy of the measurement. In fact, while acquiring a high number of frames does not have an impact on the *temporal* resolution within the RICS measurement, it does improve its accuracy and precision, which depends on the overall number of acquired photons. For this reason, a higher RICS accuracy can also be achieved by imaging a larger ROI or increasing the molecular brightness. If one were to consider only one frame, many random correlation peaks can be observed in the SACF at large ξ and ψ values, where the ACF should decay to zero (Fig. 4A-B). These side peaks are due to coincidental correlations occurring from different particles at different positions in the image and, as such, are shifted in x and y. Since these peaks are coming from random correlations, they average out when the sampling becomes large enough and the SACFs decay to zero as expected (e.g. after 10 frames as shown in Fig. 4A). The quality of the correlation improves when more than 10 frames are acquired, yet Brown et al. showed that, when enough photons are recorded, there is no great advantage in acquiring 300 frames over 50 (Fig. 4A-B) [38]. In the context of live cell imaging, the possibility of acquiring a lower number of frames is advantageous for reducing photobleaching and phototoxicity. This also enables one to acquire multiple datasets of lower-number, opening the possibility of performing kinetics studies, i.e. following how molecular properties such as diffusion, concentration, and conformational changes vary over time. Here, the number of frames collected for the SACF calculation directly influences the time resolution of the measured kinetics. For a typical RICS experiment, 50–100 frames are sufficient.

2.1.4. ROI size

From a technical point-of-view, the number of frames to be acquired should also take into consideration the size of the scanned region. Indeed, fewer frames are sufficient for larger regions of interest and vice versa (Fig. 4C). The accuracy of information extracted from SACFs calculated on very small ROIs is undermined by insufficient sampling. This is due to an impaired estimation of the mean intensity - a parameter that directly impacts the accuracy of the ACFs, as it constitutes its denominator (Eq. (6)). Improving the estimation of the mean intensity by including the average value of all the pixels in the ROI over a range of images enabled Longfils et al. to analyze ROIs down to 6 × 6 pixels without compromising the SACF accuracy [37].

2.1.5. Molecular brightness

The molecular brightness also plays a role in determining the optimal number of frames. The predicted data of Longfils and colleagues showed that, for a very high molecular brightness (≥ 100 kHz), 20 images are more than enough for a high quality SACF. This means that, if photobleaching of the sample is not a concern, one can image at high laser power, increasing the molecular brightness, and calculate the SACF on as little as, e.g., 5 frames [38]. However, photobleaching is a common problem, especially when dealing with fluorescent proteins, which means that a typical experiment is performed at lower laser powers and brightnesses of ~10 kHz are more typical. In this case, the optimal frame number increases to 100 [37].

2.2. Detrending RICS data

In a RICS analysis, every source leading to spatial intensity fluctuations, whether they are originating from translational diffusion, from stationary structures or from a non-homogeneous distribution of the molecules within the cell, will correlate. Thus, before performing correlation analyses, an image intensity homogenization step is often required to remove, for example, stationary or slowly moving bright or dark objects, or simple concentration-related intensity heterogeneities from the image. This is especially important in cells where the presence of large immobile structures would dominate the ACF and mask the underlying molecular dynamics (Fig. 5A-D). The first proposed method to filter out the immobile components was to calculate an average image over the whole image stack and then subtract it from each frame [17]. However, due to normal cellular movements, no structure remains perfectly immobile during the entire movie and, thus, they cannot be fully removed with this approach. To account for slow cellular movements, a *moving average* subtraction has been implemented and is typically used [38]. With this method, the average image is calculated not over the whole image stack, but only across a range of a few consecutive frames. This average image is then subtracted from the image of interest in the middle of the frame range. Practically, performing a moving average subtraction using 3 frames means that the average of frames 1 to 3 is subtracted from frame 2. After subtraction, the average image intensity of the entire stack (i.e. averaged in both space and time, which is a constant value), is then added back to all pixels of each frame to avoid negative values. This method however introduces a bias in the SACF amplitude. Since the fluctuations of interest are also included in the subtracted average image, the SACF amplitude will be reduced. To correct for this, the SACF should be rescaled according to [40]:

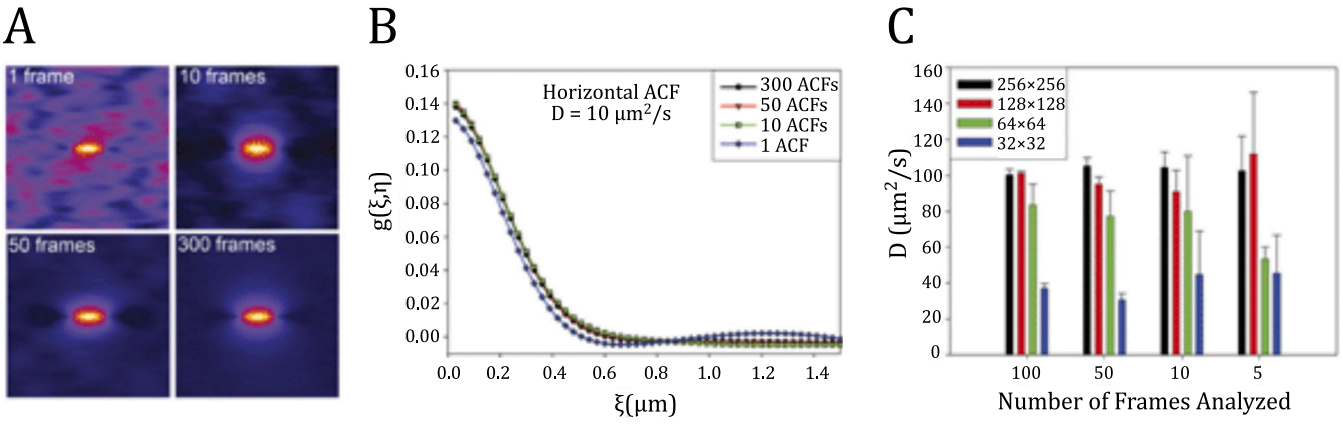

Fig. 4. Effect of frame number and ROI size on the accuracy of RICS experiments. Reproduced with minor formatting changes from [38], © 2007 The Authors. Journal compilation © 2007 The Royal Microscopical Society, Journal of Microscopy, 229, 78–91. A) 2D-ACFs obtained by averaging different numbers of frames. Averaging 10 frames already greatly reduces the random correlation peaks that appear distant to the central correlation peak, where the ACF should decay to 0. Reproduced from [38], Fig. 4B. B) x-dimension of the ACFs calculated in (A). Reproduced from [38], Fig. 4C. C) Effect of ROI size and number of analyzed frames on the estimation of the diffusion coefficient of EGFP in solution. A reasonable estimation can be obtained within 5 to 10 frames, when the ROI is sufficiently large (128 × 128 pixel, in this case corresponding to 2.94 × 2.94 μm). Reproduced from [38], Fig. 7D.

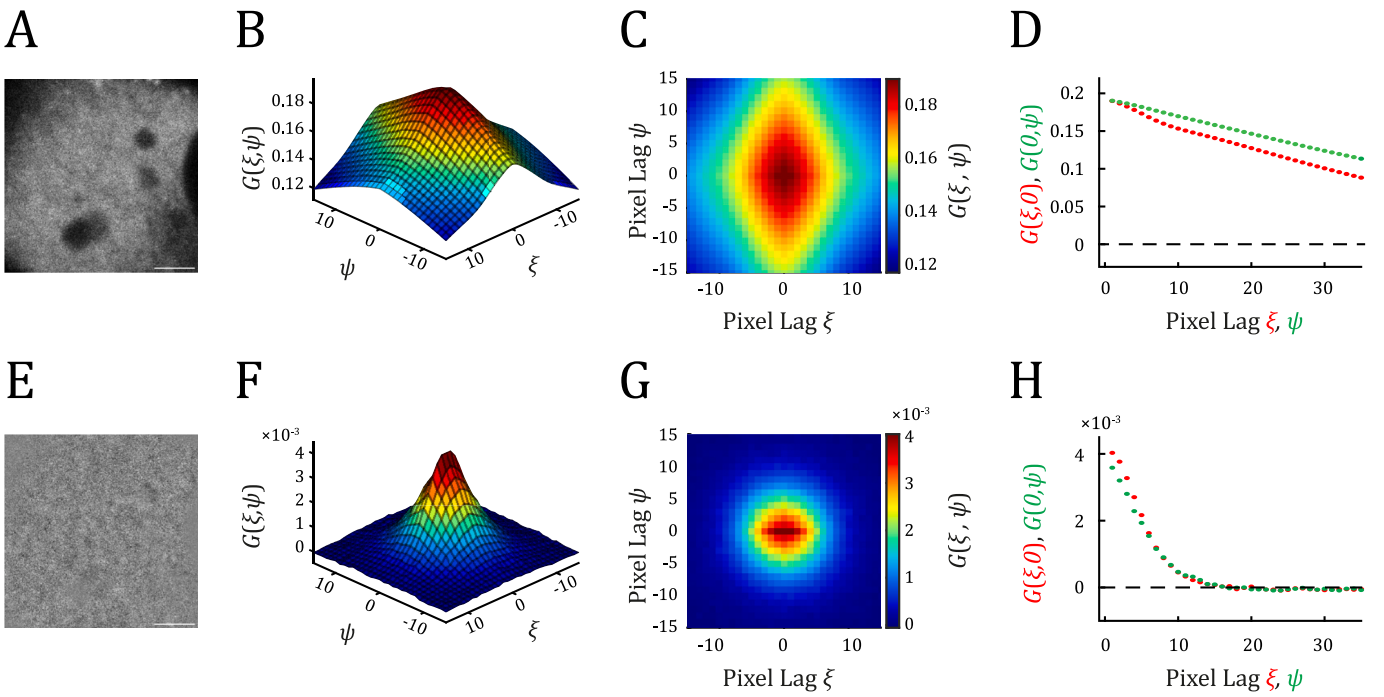

Fig. 5. The effect of detrending data on RICS analyses. A) Confocal image of a HeLa cell expressing the HIV-1 protein Gag-tagged with mCherry. The cells were transfected 18 h before imaging with X-tremeGENE™ 9 DNA (Roche) and the data were acquired at 37 °C acquired using raster scanning as described in [23], with a pixel dwell time of 11 µs, line time of 3.3 ms and pixel size of 40 nm. Scale bar: 5 µm. B) The SACF averaged over 150 frames analyzed without any preprocessing using the MIA submodule of PAM software is shown [31]. As expected, the shape of the SACF is dominated by static cellular structures. C) A top view of the SACF shown in (B). D) One-dimensional slices through the SACF in (B). Red curve: $G(\xi,0)$, green curve: $G(0,\psi)$. E) The image in (A) corrected for static components by subtracting a +/− 1 frame moving average and adding back the average image intensity of the entire stack. With this correction, the spatial inhomogeneities of the original image are mitigated. F) The SACF computed from the corrected images. Here we can see that the static components are no longer present in the correlation function and the diffusion coefficient of Gag-mCherry can be extracted and is equal to 0.55 µm^2/s. G) A top view of the SACF shown in (F). H) One-dimensional slices through the SACF in (F). Red curve: $G(\xi,0)$, green curve: $G(0,\psi)$. (For interpretation of the references to color in this figure legend, the reader is referred to the web version of this article.)

$$G_{corr}(\xi,\psi) = \frac{n}{n-1} G(\xi,\psi) \tag{14}$$

with n being the number of frames used for the moving average (indicated as $2\Delta F + 1$ by Hendrix et al., 2016). Practically, it is sufficient to take a moving average of +/− 1 frame. With this method the immobile structures of the cells are effectively removed from the image and the correlation is representative of the underlying molecular motion (Fig. 5E-H).

An alternative approach for filtering a dynamic background was proposed by De Mets and colleagues based on cross-correlation between two adjacent images [41]. This method assumes that fast moving components are *not* correlated between frames while stationary structures, i.e., immobile components imaged over several frames, will correlate. With this in mind, the immobile structure will show up in the cross-correlation between one image and the next in the image stack. Therefore, the cross-correlation between each frame i and the next $(i+1)$ is calculated and averaged over the entire stack. The autocorrelation is also calculated for each frame i and averaged over the image stack. The averaged cross-correlation function is then subtracted from the averaged autocorrelation function, which enables removal of the contribution from immobile components. The cross-correlation subtraction is similar to a moving average subtraction performed over $n = 2$ frames and allows efficient filtering of structures that move faster.

2.3. Single-photon counting versus analog detection

RICS is a versatile technique for obtaining spatiotemporal information about dynamic processes in the microsecond-to-second timescale, placing itself between single-point FCS and other ICS methods such as TICS. One of the main advantages of RICS is that it can be performed also with commercially available laser scanning confocal microscopes, making it accessible to most life-science researchers [37,38]. RICS can be done using both analog and single-photon-counting detection. With analog detection, the electrical inputs coming from different photons are integrated over time, generating a continuous output current proportional to the intensity of the light signal. On the other hand, with single-photon-counting detection, each detected photon is converted into a single electronic pulse [42]. Care should be taken as some commercial manufactures convert the analog signal into an effective number of photons, but do not do real photon counting and should be treated as an analog system. In analog mode, the electronic noise is included in the output signal while, in photon-counting mode, a so-called pulse height discriminator sets a detection threshold to separate photon signal from noise. Thus, photon counting has a better signal-to-noise ratio at low light intensities making it more suitable under these conditions [43]. Single photon counting is usually preferable for FCS and RICS not only due to the higher sensitivity, but also because integration of the signal in analog detection can introduce unwanted correlations, i.e. the detector noise can be correlated. This can become a problem at higher scan speeds where the detector electronics do not have enough time to fully reset itself before acquiring the next data point. In other words, the time scale of the detector correlations is on the order of the pixel dwell or longer. This leads to unwanted correlations between pixels along the x-axis [38,44]. However, correcting these correlation artifacts is relatively easy: one needs to exclude both the zero lag point $G(0,0)$ and a few surrounding points along the x-axis of the SACF before fitting. As the detector noise depends on the detector itself, the number of points to skip must be determined independently for each detector. This can be done by measuring and correlating dark counts, i.e. collecting images

with no sample in place and no light reaching the detector [39]. Detailed noise characterization has been done for a number of different setups such as the Olympus Fluoview 300 (FV300) [38], Zeiss LSM510 META [44] and Nikon C1 [45]. In the case of single photon counting, dark counts and background will still correlate at zero lag, which is why the $G(0,0)$ point is always excluded when analyzing RICS data.

3. Direct detection of molecular interactions with cross – correlation RICS

A common approach in biology to measure the association between two molecules is to label them with different fluorophores and evaluate their colocalization, i.e. the overlap of their respective fluorescent signals within the cell. Different methods can be used to assess the colocalization, both pixel-based (Pearson's correlation coefficient, Mander's split coefficient) or object-based. However, unless super-resolution microscopy is employed, all colocalization methods are limited by the optical resolution of the system, typically $\gtrsim$ 200 nm. When two molecules are within a proximity of ~200 nm, they will be considered as colocalized. Since 200 nm are a relatively large distance in the molecular scale, colocalization will not necessarily indicate an interaction or association, and can lead to false positive results. Another common technique to assess molecular association is FRET, which is sensitive to distances of $\lesssim$ 10 nm and, therefore, is a more accurate predictor for interactions. However, if the molecules are associated but the fluorophores are located at a distance greater than 10 nm, there will be no FRET signal and the result will be a false negative.

The abovementioned limitations can be addressed by dual color RICS, an extension of the RICS method that can be performed when two different spectral detection channels are implemented. With this approach, one cannot only analyze the SACFs of the two individual channels, but also perform a cross-correlation RICS analysis (ccRICS) between the two channels [46]. A cross-correlation analysis reveals whether or not differently labeled molecules co-diffuse and, as such, is a reliable reporter for interactions. For example, ccRICS was used to show that the focal adhesion associated protein vinculin and the focal adhesion kinase (FAK), despite having overlapping intensity signal in the cytoplasm, do not actually interact in the cytoplasm, but only at the level of disassembling adhesions [46]. Overall, ccRICS can be used to investigate the formation, diffusion and spatial distribution of molecular complexes [24,27,46,47].

Before continuing with ccRICS, we briefly discuss the concept of dual-color fluorescence cross-correlation spectroscopy (FCCS) [48], from which ccRICS is derived. In a FCCS experiment, the fluorescence intensity from two differently labeled molecules are measured in two detection channels and the cross-correlation function between the two channels is then calculated using:

$$G_{1\times2}(\tau) = \frac{\langle \delta I_1(t)\delta I_2(t+\tau)\rangle_t}{\langle I_1(t)\rangle_t \langle I_2(t)\rangle_t} \tag{15}$$

where the two channels are denoted by the subscript 1 and 2. Assuming a 3D-Gaussian observation volume with identical size and perfect overlap for the two channels, the cross correlation can be analytically derived:

$$G_{1\times2}(\tau) = \frac{\gamma\langle N_{12}\rangle}{\langle N_1+N_{12}\rangle\langle N_2+N_{12}\rangle}\left(1+\frac{4D_{12}\tau}{\omega_r^2}\right)^{-1}\left(1+\frac{4D_{12}\tau}{\omega_z^2}\right)^{-\frac{1}{2}} \tag{16}$$

here, $\langle N_{12}\rangle$ indicates average number of complexes in the confocal volume detected in both channels. Similarly, in a ccRICS experiment, two detection channels are (and must be) acquired simultaneously (at least within the pixel time), i.e. the sample is scanned at the same time by both excitation lasers and the emission of the two different fluorophores are collected by two synchronized detectors. A cross-correlation will be detected only when a signal fluctuation occurs in both channels at the same time, for instance due to the diffusion of a double-labeled complex through the volume.

As for one-color RICS, the ccRICS spatial cross correlation function (SCCF) is calculated within the same frame. The difference is that, in RICS, the spatial autocorrelation is calculated by multiplying the image by a shifted copy of itself while, in ccRICS, the spatial cross-correlation is obtained by multiplying one image with that collected in the other channel (Fig. 6A-C):

$$G_{ccRICS}(\xi,\psi) = \frac{\langle \delta I_1(x,y)\delta I_2(x+\xi,y+\psi)\rangle_{x,y}}{\langle I_1(x,y)\rangle_{x,y}\langle I_2(x,y)\rangle_{x,y}} \tag{17}$$

In a typical experiment, with a 1:1 binding stoichiometry, the maximum amplitude of the cross correlation is dictated by the amplitudes of the autocorrelation in channels 1 and 2. As such, $G_{cc}(0,0) \leq G_{1\ or\ 2}$. However, for different binding stoichiometries, the amplitude of the cross-correlation function may exceed the amplitude of the autocorrelation functions, as discussed by Kim and colleagues with respect to FCCS [49]. As for FCCS, the amplitude of the cross-correlation can be affected by several factors such as imperfect overlap of the observation volumes, FRET occurring between the two fluorophores, dark states of the fluorophores caused by photobleaching or misfolding, and spectral crosstalk [50]. The various strategies that have been employed to address the issue of spectral crosstalk will be discussed later.

CcRICS is a powerful tool for investigating interactions. The interactions need to occur within a single image, so on the time scale of ~1 s. Hence, it can be used to follow dynamic changes in interactions such as degradation kinetics at the single-cell level. For example, Sasaki and colleagues utilized ccRICS to directly evaluate the different timing of exogenous DNA degradation in different cell lines [27]. They injected cells with a double-labeled, double-stranded DNA and monitored the decrease of cross-correlation over time as a readout of DNA degradation (Fig. 6D, E). With these experiments, they could show that mouse embryonic fibroblast (MEF) cells degrade exogenous DNA much faster than human embryonic kidney (HEK293) cells, possibly due to higher contents and/or activity of cytoplasmatic nucleases. When placed in the context of gene delivery and gene therapy, this result suggests that different DNA delivery approaches should be considered for different cell lines, to minimize degradation and maximize gene expression.

4. RICS versus FCS for live-cell measurements

In the context of live-cell imaging, RICS presents some advantages over classical FCS. One intrinsic benefit of RICS is the acquisition of an image instead of a time trace collected at a single location without information about the surroundings. This allows one to observe cellular structures and potentially to analyze the diffusion dynamics in different regions of the cell, e.g. in the cytoplasm versus in an organelle, within a single experiment. At the same time, determining the diffusion coefficients from a larger area of the cell helps mitigate the impact of local heterogeneities, which can significantly affect FCS results.

Several approaches have been implemented over the years to increase the spatial sensitivity of FCS measurements. The first method developed was scanning FCS [7–9], in which one line (or orbit) is scanned multiple times. While this increases the probe volume, it may still be insufficient to capture the heterogeneity of a complex system. To increase the area monitored in an FCS experiment, it has been combined with a electron multiplying charged coupled detector (EMCCD). This allowed a significant increase the imaging area, but with a significant compromise in the time resolution to milliseconds or hundreds of microseconds at best. EMCCD-based FCS has been realized in epifluorescence [51], total internal reflection (TIR) illumination [52,53] and spinning disk confocal microscopy [54,55]. Here, multi-focal FCS is realized by using a stationary Nipkow disk to create an array of focal points that give rise to tens or hundreds of FCS-like measurements. Notably, using only limited areas of the EMCCD chip enables a faster

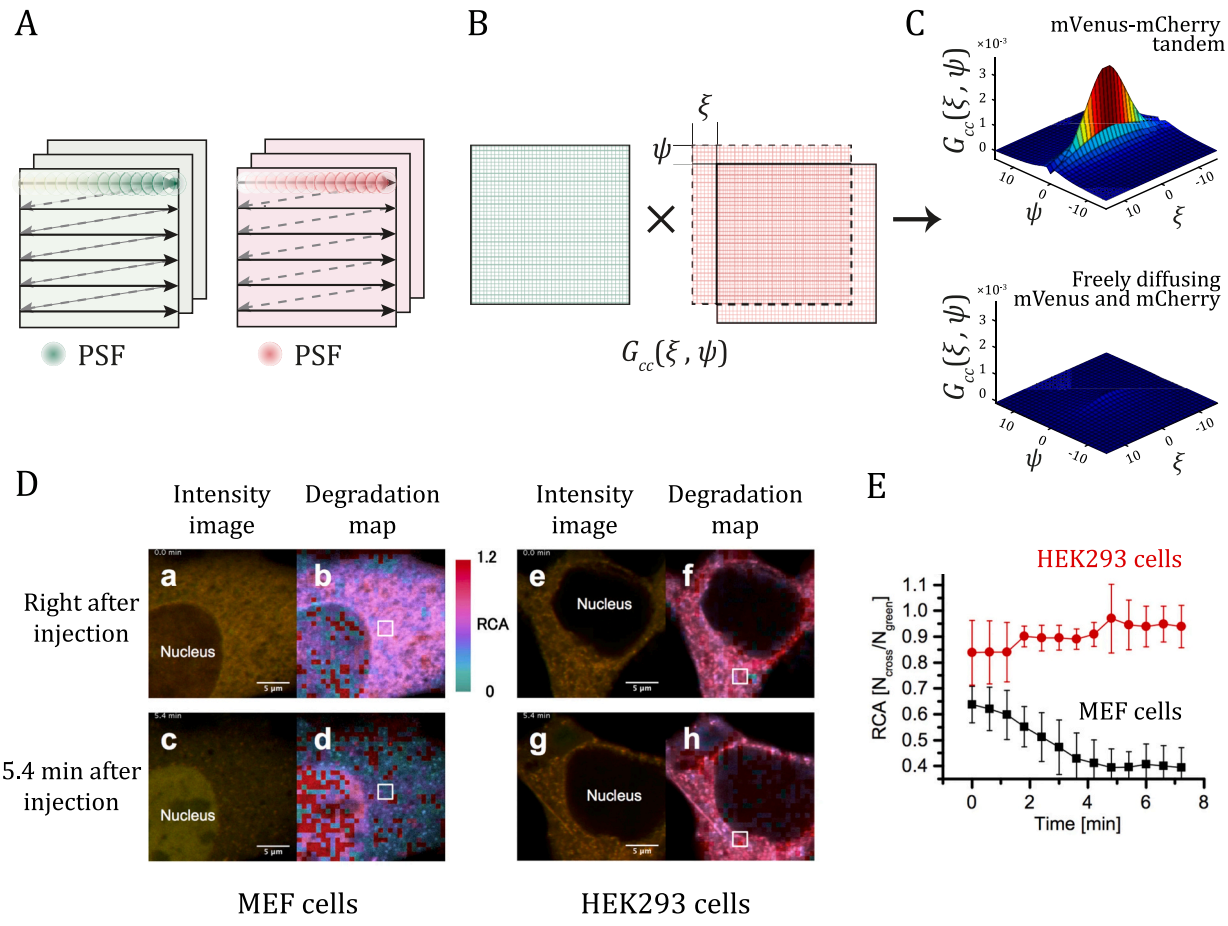

Fig. 6. Principle and application of cross-correlation RICS. A) Schematic of image acquisition by raster scanning in two channels. B) Graphic representation of the cross-correlation calculation. Each frame of the first channel is multiplied by the corresponding frame in the second channel, shifted by a pixel lag (ξ, ψ). C) Example of a 2D spatial cross-correlation function for fluorescent proteins diffusing in the cytosol of HeLa cells. The cross-correlation can only be detected when mVenus and mCherry are linked together as a tandem construct (top panel) and not when the two proteins are free to diffuse independently (bottom panel). The cells were transfected 18 h before imaging with X-tremeGENE™ 9 DNA (Roche) and the data were acquired at 37 °C on a raster scanning confocal microscope as described in [23] with a pixel dwell time of 11 µs and analyzed with PAM (MIA submodule) [31]. (D, E) CcRICS analysis of DNA degradation in living cells. Adapted and reproduced from [27], Fig. 5A-I, under the terms of the Creative Common Attribution 4.0 Int. (CC-BY 4.0) License (http://creativecommons.org/licenses/by/4.0/). D) Confocal images and degradation maps of double-labeled DNA injected into MEF and HEK293 cells. The degradation maps depict the relative cross-correlation amplitude (RCA). E) Degradation of double-labeled DNA over time in MEF (black) and HEK293 (red) cells. The RCA was calculated in nine different ROIs, an example of which is represented by the white squares in panel (D), and the mean and standard deviations are plotted. (For interpretation of the references to color in this figure legend, the reader is referred to the web version of this article.)

readout rate and the use of a cumulant analysis increased the time resolution to that of the exposure time of 20 µs [56]. Multi-focal FCS with confocal illumination can also be performed using a single-photon avalanche photodiode (SPAD) array as a detector [57–60]. In this setting, a continuous-wave (CW) laser beam is expanded and directed onto a diffractive optical element (DOE), generating a diffraction pattern of 32 × 32 well separated spots that illuminate the sample. The fluorescence emission is then imaged on the SPAD array giving rise to 32 × 32, i.e. 1024, FCS curves. SPAD-based FCS can reach a time resolution of 20 µs. However, due to prevalent afterpulsing in this detector, the effective time resolution of the ACF was limited to 100 µs [58]. Overall, multi-pixel -based FCS methods offer a valid compromise between the fast time resolution of classical FCS and the high spatial resolution of image correlation spectroscopy, but present technical challenges that should be carefully taken into consideration. Compared to multi-focus FCS techniques, RICS has the advantage of providing contiguous pixels in an image, offering a more comprehensive view of the sample. However, for investigating fast processes on the nanosecond timescale such as molecular rotation, classical FCS remains preferrable, especially for samples in which cellular heterogeneities are negligible.

Another advantage of RICS is distributing the excitation light over a broad area, instead of focusing it on a single point, which avoids highly localized phototoxicity and photobleaching. Nowadays, a few cell-permeable organic dyes have been developed, but the fluorophore of choice for live-cell imaging is still often fluorescence proteins, which are known to be highly sensitive by photobleaching. Fluorescence proteins, especially green and yellow shifted ones, are also affected by other fast photophysical phenomena (i.e. blinking) [61,62]. Interestingly, adding a blinking term to the RICS fitting equation allows for a robust determination of the diffusion coefficient of the Venus fluorescent protein even at high laser powers where severe photobleaching and blinking are induced, enabling it to outperform FCS [63]. TIR illumination and light sheet microscopy can be used to greatly reduce photobleaching. The implementation of FCS with TIR microscopy is typically realized with EMCCD cameras, leading to limited time resolution discussed above [52,53]. However, TIR illumination can be combined with point detectors as was demonstrated by Ohsugi and Kinjo who reached a time resolution of 3 µs at seven positions simultaneously using photomultiplier tubes (PMTs) [64]. Light sheet microscopy is particularly advantageous for imaging living tissues, embryos and organoids [65]. Light-sheet based FCS was used to investigate blood flow in zebrafish embryos [66] as well as the diffusion of GFP fused to the nuclear

localization signal (NLS) sequence in the imaginal discs of Drosophila's larvae [67]. When combined with SPAD detection, light-sheet FCS can reach a time resolution of 20 μs [68].

5. Dealing with the spatial averaging of RICS

The intrinsic ability of RICS to gather dynamic information from images of the cell allows investigations of molecular diffusion in different areas of interest by dividing the image (and then the analysis) into specific ROIs. However, since the diffusion coefficient obtained from fitting the SACF is the average value over the analyzed region, RICS analyses assume constant properties of molecules within a given ROI [17]. This is a significant disadvantage of the original RICS method, not only because the presence of bright aggregates or contamination can heavily skew the SACF, but also because averaging the information over space precludes the possibility of generating pixel-based diffusion and/or concentration maps. To overcome these limitations, a few strategies have been developed over the years. The initial approach consisted in simply dividing the image into smaller subregions and calculating the SACF for each of them [44]. Subsequently, Hendrix et al. implemented an arbitrary-region RICS (ARICS) algorithm that allows one to select non-squared, dynamic ROIs [40]. In 2018, Scipioni et al. proposed a strategy named local RICS (L-RICS), an ICS segmentation method based on the analysis of the *x*-axis component of local SACFs to generate high resolution diffusion maps [69]. Additionally, the spatial resolution of RICS was further increased by Hedde et al., who combined RICS with stimulated emission depletion (STED), developing the STED-RICS technique [70]. These approaches are described in more detail below.

5.1. Spatial mapping of the diffusion coefficient with a grid based RICS analysis

In 2009, Gielen and colleagues proposed an approach to obtain a more detailed landscape of diffusion coefficients within an image [44]. Their idea was very straightforward: to improve the spatial resolution, they subdivided the image into smaller squared ROIs with the help of a grid pattern. A SACF was then calculated from each ROI and the resulting D was used to generate a map of diffusion coefficients. With the support of simulated data, they analyzed the impact of a progressively smaller ROI size on the accuracy of the retrieved diffusion coefficient and could show that a ROI as small as 32 × 32 pixel (corresponding in their case to 1.76 × 1.76 μm) can give reliable and reproducible results. This approach proved useful to map the diffusion of liposomes under the *stratum corneum* of the human skin, a tissue characterized by high structural heterogeneities [71]. Sasaki et al. applied a similar approach to analyze DNA degradation (Fig. 6D). In their case, they subdivided their images into 32 ROIs of 64 × 64 pixels and analyzed the auto- and cross-correlation functions of a double-labeled DNA molecule in each of these ROIs. By mapping the relative cross-correlation amplitude (RCA) of each ROI onto the confocal images, they could generate DNA degradation maps in living cells [27].

The increase in spatial resolution provided by this method presents some limitations. To obtain enough statistics with a small ROI, one needs to acquire a higher number of frames to obtain accurate diffusion coefficients [38]. This constraint leads to longer imaging times and consequently a higher chance of photobleaching the sample. In addition, with the smaller the grid element, the more the average intensity is improperly sampled, introducing a non-negligible, systematic estimation bias. Longfils et al. recently propose a way to correct this by estimating the average intensity $\langle F \rangle$ not on a single grid unit but on a larger scale, which allows one to obtain reliable diffusion coefficients for ROIs as small as 6 × 6 pixels [37].

5.2. RICS using image segmentation

The classic algorithm used for analyzing ICS (and RICS) data is based on square regions of interest. This is necessary when one wishes to use a Fast Fourier Algorithm for calculating the correlation function. For a fluorescence intensity image I of size $X \times Y$, the SACF is defined as [15]:

$$G(\xi,\psi) = \frac{\sum_{x,y}\delta I(x,y) \times \delta I(x+\xi, y+\psi)}{\langle I(x,y)\rangle_{x,y}^2} \times \frac{1}{(X-|\xi|)(Y-|\psi|)} \tag{18}$$

with the denominator representing the number of times a particular spatial lag (ξ,ψ) can be sampled, which is maximum at a spatial lag of $(0,0)$ and decreases as the spatial lag in x and/or y increases. $G(\xi,\psi)$ is then normalized by the intensity squared, as in Eq. (6). However, a squared region of interest is not suitable to study diffusion in cellular compartments with complex shapes such organelles or membranes. For this reason, Hendrix et al. implemented a generalization of Eq. (18) to allow the correlation to be calculated on arbitrarily shaped ROIs [40,72]. First, a ROI mask $R(x,y)$ is defined in which pixels have a value 1 inside the mask and 0 outside the mask (Fig. 7A-C). To exclude pixels outside the ROI from the correlation, each pixel of the original image is multiplied with the corresponding pixel in the mask. In this way, the intensity fluctuations are redefined as:

$$\delta I_R(x,y) = R(x,y)\left(I_R(x,y) - \langle I_R\rangle_{x,y}\right) \tag{19}$$

with $\langle I_R\rangle_{XY}$ being the average intensity of the pixels inside the ROI. Also in this case, the SACF needs to be normalized over the number of times the spatial lag can be sampled. This is conveniently given by the correlation of the mask. Taken together, the generalized SACF becomes:

$$G(\xi,\psi) = \frac{\sum_{x,y}\delta I_R(x,y) \times \delta I_R(x+\xi, y+\psi)}{\langle I_R(x,y)\rangle_{x,y}^2} \times \frac{1}{\langle R(x,y) \times R(x+\xi, y+\psi)\rangle_{x,y}} \tag{20}$$

Note, $G(\xi,\psi)$ has been normalized over the mean square intensity of the pixels inside the mask $\langle I_R\rangle^2_{x,y}$ and averaged across all frames. With the introduction of this new, arbitrary-region RICS (ARICS) algorithm, RICS images are no longer limited to 2^n pixels structures, as has been traditionally the case for other ICS methods. ARICS has been implemented in the Microtime Image Analysis (MIA) submodule of the analyses software PIE Analysis with MATLAB (PAM) [31]. The ROI selection is very flexible and can be done in several ways, including being selected with a free hand drawing or intensity thresholding. It can also be performed dynamically, changing the ROI in each frame according to, for example, fluorescence intensity variations. This allows one to correct, for instance, for bright aggregates diffusing through the image series, which will otherwise heavily affect the correlation function. The ROI can also be selected on a second imaging channel where a structure of interest, such as an organelle, is labeled. Recently, this approach was used to evaluate the diffusion of histone H3.1 in the nucleoplasm and inside pericentromeric heterochromatin regions in living mouse embryos [73]. ARICS was applied to create ROIs delimiting the heterochromatin region, labeled with mClover. The diffusion of SNAP-labeled H3.1 was measured and found to be slower in the pericentromeric heterochromatin in both 2-cell and 4-cell stage embryos, suggesting that these domains behave as membrane-less compartments (Fig. 7D-F).

In ARICS, multiple ROIs can also be combined by pixelwise multiplication. The possibility of selecting many different ROIs in the same image gives the opportunity to investigate diffusion in different cellular compartments at the same time. This feature can be exploited to generate diffusion and/or concentration pseudo-maps. Hendrix and colleagues used the fluorescence intensity of a chromatin density marker (H2B-mRFP) to define five ROIs based on the fluorescence intensity of the marker in the original ARICS publication [40]. In the other channel, the SACF of the protein of interest, LEDGF/p75-eGFP, was calculated. After fitting the SACF in each ROI, the N and D obtained were spatially computed. The results showed that the concentration of LEDGF/p75

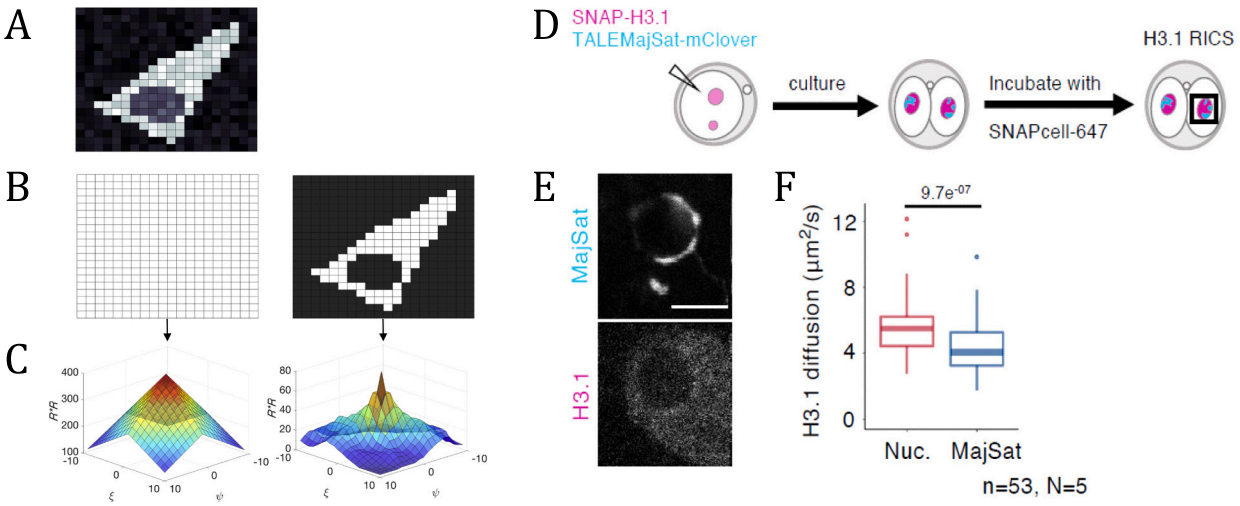

Fig. 7. Arbitrary RICS concept and implementation. (A-C) Comparison between a squared and a generalized, arbitrary ROI. Reproduced from [40], Fig. 1A-E, under the terms of the Creative Common Attribution-Noncommercial-Nonderivatives 4.0 Int. (CC-BY-NC-ND 4.0) License (https://creativecommons.org/licenses/by-nc-nd/4.0/). A) Schematic representation of a 20 × 20 pixels intensity image of a cell with high fluorescence intensity in the cytoplasm. B) Comparison between the full, square ROI (left) used in a classical RICS algorithm, where all the pixels of the image in (A) are selected and correlated, and an arbitrary ROI (right) in which only pixels corresponding to the cell cytoplasm are considered for the analysis. The arbitrary ROI is obtained by intensity thresholding. C) SACFs of the square and arbitrary ROIs, indicating the number of times a particular spatial lag is sampled. This value corresponds to the denominator of the SACF (Eq. (18) for classical ICS, Eq. (20) for ARICS). (D-F) Diffusion of histone H3.1 inside and outside chromocenters in mouse embryos. Reproduced from [73], Fig. 2B, under the terms of the Creative Common Attribution-Noncommercial 4.0 Int. (CC-BY-NC 4.0) License (http://creativecommons.org/licenses/by-nc/4.0/). D) Schematic of the experimental workflow: Mouse embryos were injected with mRNA for SNAP-H3.1 to label the histone and TALEMajSat-mClover to label the chromocenters. The embryos were incubated until the two-cell stage and stained with SNAPcell-647 to label the SNAP-for the RICS experiment. E) Representative confocal images of the chromocenter (MajSat) and histone H3.1. F) Diffusion of H3.1 inside and outside the chromocenter. ARICS was employed to generate a mask of the chromocenters via intensity thresholding of the MajSat detection channel. The mask was applied to the H3.1 channel and ARICS was performed on the region inside and outside the mask.

correlates with chromatin density, while the diffusion of LEDGF/p75 is faster in regions of lower chromatin density, except for inside the nucleoli, in which low chromatin density is associated with lower mobility.

ARICS can also be used to remove unwanted artifacts from an image series. In the presence of bright aggregates that move from frame to frame, a simple moving-average subtraction of +/− 1 frame will not be sufficient. However, it is possible to generate an arbitrary ROI by using intensity thresholding to filter out the high intensity pixels coming from the bright particles, de facto excluding those aggregates from the RICS

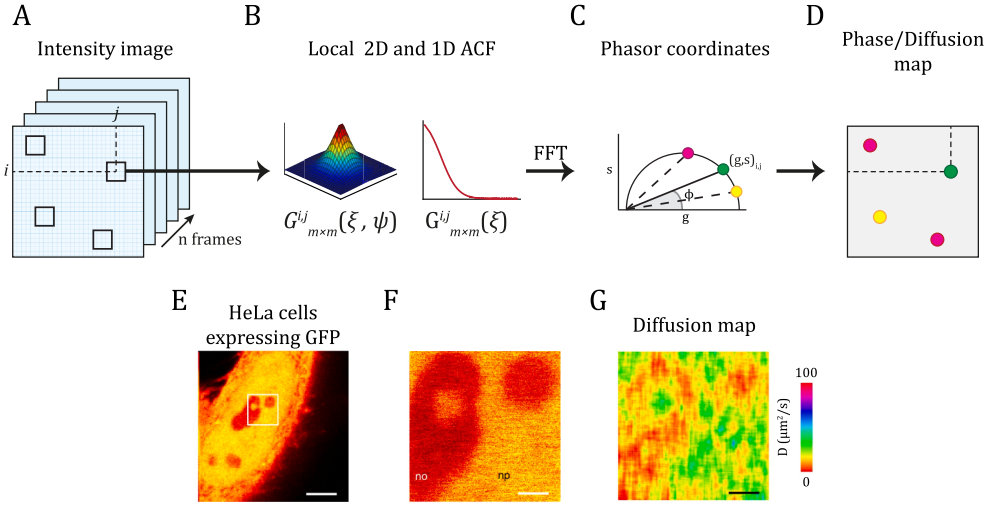

Fig. 8. Illustration of the local-RICS principle and its application in live cells. (A-D) Schematic illustration of the L-RICS methodology. A) Several frames are acquired by a raster-scanning confocal microscope. B) The local ACF is calculated from a small m × m ROI for every pixel (i, j) of an image, which is then averaged across n frames. The 1D ACF is obtained by considering only the x -direction of the correlation (the ξ lag). C) The phasor coordinates (g, s) are calculated from the 1D ACF by a fast Fourier transform (FFT). The phase angle of the phasor diagram is represented by ϕ. D) Diffusion maps generated by plotting the local diffusion coefficient $D_{(i,j)}$ obtained from the respective $\phi_{(i,j)}$ value. The relationship between ϕ and D has been characterized with simulated data by Scipioni et al. [69]. (E-G) Diffusion of GFP in the nucleus of HeLa cells, adapted and reproduced from [69] (original Fig. 4A) under the terms of the Creative Common Attribution 4.0 Int. (CC-BY 4.0) License (http://creativecommons.org/licenses/by/4.0/). E) HeLa cells expressing GFP, scale bar 5 μm. L-RICS is performed on the 256 × 256 pixels area enclosed in the white square. F) Enlarged view of the L-RICS area in panel (E), in which both the nucleolus (no) and nucleoplasm (np) are visible. The scale bar is 1 μm. G) Diffusion map obtained by performing an L-RICS analysis of the area in (F), averaging the local ACFs across 100 frames.

analyses.

5.3. Local RICS

To achieve sub-micrometer resolution without reducing the ROI size, Scipioni and colleagues combined the previously established phasor analyses of local ICS [74] with the RICS method, introducing local RICS (L-RICS) [69]. L-RICS achieves high spatial resolution by determining many local spatial ACFs, calculated on very small regions around every pixel of the image set. Since fitting the large number of generated ACFs would be computationally challenging, the local ACFs are analyzed via the phasor approach, a fit-free method originally developed to analyze fluorescence lifetime imaging data [75–78]. Briefly, for each pixel (i,j) in an image, a local SACF is calculated within a very small $m \times m$ ROI and transformed into Fourier space by applying a fast Fourier transform (FFT) (Fig. 8A-B). The result is then averaged over the total number of frames. The sine and cosine Fourier components of the transformation are the *s* and *g* phasor coordinates, which define the modulation (M) and phase (ϕ) of the phase vector (Fig. 8C). With the aid of simulated diffusion data, Scipioni and colleagues built a calibration curve for the phase parameter, thus establishing a precise relationship between ϕ and the diffusion coefficient. In this way, the phase parameter of each pixel $\phi_{(i,j)}$ can be used to generate a diffusion map (Fig. 8D). By using the L-RICS method, they could generate diffusion maps with sub-micrometer resolution showing the high degree of heterogeneity of GFP inside the nucleus of HeLa cells (Fig. 8E-G). In addition, they could show differences in diffusion coefficients even within the nucleolus, which could reflect heterogeneity in chromatin compaction.

5.4. STED-RICS

Another way to achieve sub-micrometer resolution with RICS is to combine it with super-resolution methods such as STED microscopy [79,80] similarly to what was previously done for FCS [70,81]. STED microscopy is realized by co-aligning the excitation beam with a second, red-shifted STED beam with a doughnut-shaped illumination profile. This is typically achieved by using a vortex phase plate, with a zero-field in the center and maximum intensity in the periphery. The high intensity of the STED laser depletes excited fluorophores in the periphery of the excitation profile, leaving only the fluorophores in the center to emit light and thus contribute to the image. The size of the observation volumes is determined by the power of the STED laser: the higher the intensity, the larger the depletion area and therefore the smaller the observation volume. In FCS and RICS, the size of the observation volume dictates the upper concentration limit, usually in the tens of nanomolar regime. When too many molecules are present in the observation volume, the magnitude of single molecule fluctuations will be very small and it becomes difficult to distinguish meaningful fluctuations from other noise sources. However, when the observation volume is reduced, less molecule will be in the focus at the same concentration, thus allowing detection of single molecules fluctuations even in highly concentrated samples. Combining FCS and RICS with STED gives the possibility of tuning the observation volume according to the sample concentration, which can be extended by a factor of 10–100 compared to classical RICS experiments [81]. This can be especially useful for live-cell imaging experiments where the fluorophore concentration can be difficult to control. In addition, Hedde et al. showed that, with STED-RICS, the ROI size can be reduced to 640 × 640 nm^2 without incurring artifacts. Hence, STED-RICS is a powerful technique to generate sub-micrometer resolution diffusion maps to unravel the heterogeneity of molecular dynamics in living cells.

It should be noted that the choice of fluorophores for STED-RICS, and STED in general, is crucial. The fluorophores should not absorb at the wavelength of the STED-laser to avoid rapid photobleaching caused by the high laser intensity required for depletion. Due to the low number of fluorophores in the observation volume, the fluorophores need to be very bright and photostable in order to achieve a sufficiently high signal-to-noise ratio. For live-cell imaging applications, GFP and YFP exhibit an adequate quantum yield and their use for STED microscopy has been long established [82]. However, GFP and YFP require 480 nm excitation and 595 nm depletion, while a more red-shifted, less energetic, wavelength would be more desirable for live-cell applications. Recently, far-red proteins suitable for STED have been engineered [83,84]. Organic dyes outperform fluorescent proteins, thanks to their enhanced photostability, brightness and quantum yield. Fortunately, with the advent of cell permeant dyes such as silicon rhodamine or dyes from Janelia Farm, and self-labeling protein tags such as SNAP- and Halo-Tags, organic dyes can nowadays also be used for live-cell imaging. The panel of fluorescent proteins and organic dyes appropriate for STED is in constant development and has been recently been reviewed by Stockhammer et al. [85].

Recently, STED-RICS was applied to investigate lipid mobility at the plasma membrane. Bernabé-Rubio and colleagues developed a method called laser interleaved confocal RICS and STED-RICS (LICSR), in which the laser excitation is interleaved line by line between confocal and STED modalities [86]. In this way, they could quasi-simultaneously acquire standard RICS and STED-RICS data and thus probe diffusion in different-sized observation volumes. It has been previously shown that the apparent diffusion coefficient of a molecule in different observation volumes may change accordingly to its diffusion modes [87]. For a freely diffusing molecule, subjected only to Brownian motion, the diffusion coefficient will be unaffected by the spot size as the diffusion time τ_D scales linearly with the focal area ω_r^2. This is not the case for anomalous, hindered diffusion, in which τ_D increases nonlinearly with ω_r^2 due to transient interactions with the surroundings [88]. The smaller the spot size, the larger the influence of the transient interactions on the measured diffusion coefficient (Fig. 9A). Therefore, for hindered diffusion, the diffusion coefficient obtained by STED-RICS ($D_{STED-RICS}$) will be smaller than the one obtained by RICS (D_{RICS}). Hence, non-Brownian diffusion can be easily identified by taking the ratio between $D_{STED-RICS}$ and D_{RICS} with free diffusion having a $D_{ratio} = 1$ and hindered diffusion having a $D_{ratio} < 1$. By staining the plasma membrane of an epithelial cell line with a lipophilic dye, Bernabe-Rubio et al. used this approach to demonstrate that diffusion is free at the plasma membrane but hindered in lipid rafts associated with the midbody remnant (MBR) [89] (Fig. 9B). This result suggests that these regions are highly condensed and characterized by low lipid lateral mobility.

Despite its ability to enhance spatial resolution, STED-RICS remains challenging. There are the inherent technical challenges of implementing STED. In addition, the high power of the STED laser poses the obvious limitation of increased photobleaching and thus requires extremely photostable samples and limits the number of frames that can be averaged. Therefore, one needs to weigh the additional benefit of sub-micrometer resolution with the increased experimental challenges for STED-RICS.

6. Dealing with spectral crosstalk in ccRICS

While correlation methods are very powerful for investigating interactions of biomolecules, an important limitation of RICS, and especially ccRICS, is spectral crosstalk. As the fluorescence spectra of many fluorophores have a tail into the red region of the spectra, fluorescence coming from one fluorophore can be detected in the red-shifted detection channel. The amount of light emitted by the blue-shifted fluorophore and detected in the red-shifted channel is referred to as spectral crosstalk. In the absence of interacting species, spectral crosstalk will affect the red ACF and the cross-correlation function. The crosstalk CCF amplitude constitutes the minimum detectable values of the ccRICS amplitude and hampers the possibility of using ccRICS to quantify molecular interactions. Spectral crosstalk constitutes a major concern, especially for live cell imaging experiments in which the choice of labels

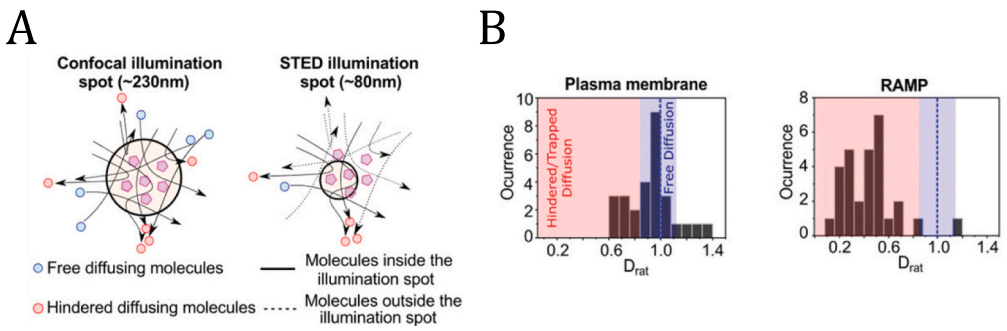

Fig. 9. Application of STED-RICS. Reproduced from Figure 3 of [86] under the terms of the Creative Common Attribution-Noncommercial-Nonderivatives 4.0 Int. (CC-BY-NC-ND 4.0) License (https://creativecommons.org/licenses/by-nc-nd/4.0/). A) Comparison between confocal-RICS and STED-RICS acquisition. With confocal acquisition, several molecules are present simultaneously in the observation volume, which can be significantly reduced by employing STED. In both cases, the observation volume is raster scanned across the sample and the resulting images are analyzed by RICS. B) Measuring free and hindered diffusion in membranes by confocal- and STED-RICS. Frequency histograms of the ratio between the diffusion coefficient measured by STED-RICS and confocal-RICS D_{rat}. At the plasma membrane (PM), D_{rat} is prevalently higher than 1, indicating free diffusion. Contrarily, at midbody associated membrane patches (RAMP), D_{rat} is predominately smaller than 1, suggesting hindered diffusion [86].

is often limited to a set of fluorescent proteins. Fluorescent proteins tend to have very broad spectra and, hence, are difficult to fully separate spectrally.

Over the years, a few strategies have been developed to overcome the crosstalk problem. A first approach is to couple RICS with pulsed interleaved excitation (PIE), a method that separates the emitted photons according to the excitation source as well as the detection channel [63,90]. Another strategy is to filter two fluorophores based on their fluorescence lifetime, with a method called raster lifetime ICS (RLICS) [63]. Finally, RICS can be combined with statistical spectral filtering, in which the fluorophores are separated based on differences in the emission spectra [91].

6.1. PIE-RICS

Pulsed interleaved excitation (PIE) is a method developed in 2005 [90] in which two or more pulsed lasers are alternated on the nanosecond timescale, reaching the sub-microsecond time resolution required to investigate translational, rotational and conformational dynamics of molecules. It is based on Alternating Laser Excitation (ALEX) developed in the group of Shimon Weiss [92,93]. In PIE, the excitation sources, picosecond to nanosecond pulsed lasers with a high repetition rate (> 1 MHz), are delayed by ~10–50 ns with respect to one another [90]. The emitted light is detected using time-correlated single-photon counting (TCSPC) electronics and, due to the synchronization of detection and excitation sources, the arrival time of the detected photons also encodes which source is responsible for exciting the molecule. This configuration allows each species to be measured independently, albeit quasi-simultaneously. After detection, the photons can be separated according to their arrival time (i.e. excitation source) (Fig. 10A). When the excitation wavelengths and emission filters are chosen wisely, it is possible to discard the photons that arise due to spectral crosstalk. For example, when green and red excitation sources are used, it is possible to cross-correlate green photons detected after green excitation with red photons detected after red excitation (*RR*). By discarding the red photons detected after green excitation (*GR*), photons due to spectral crosstalk or FRET are removed. By combining PIE and RICS [63,94,95], the false-positive cross-correlation amplitude caused by crosstalk can be completely eliminated and quantitative results from ccRICS can be obtained (Fig. 10B). Continuing with the green/red example, in the absence of PIE, the red spatial ACF is calculated for all photons detected in the red channel ($GR + RR$) and is given by:

$$G_{GR+RR}(0,0) = \left(\frac{f_{G_T,R_T}\beta^2 + 2\beta f_{GR,R_T} + 1}{\left(f_{G_T,R_T}\beta + 1\right)^2}\right)\frac{1}{N_{R_T}} \tag{21}$$

where f_{G_T,R_T} is the ratio of total green molecules over total red molecules in the observation volume, f_{GR,R_T} is the ratio of double-labeled molecules over the total red molecules and β is the crosstalk parameter, i.e., the ratio between the green and red fluorophore brightness, both calculated in the combined red channel F_{GR+RR}. N_{R_T} is the total number of red labeled molecules $(N_{R_T} = N_R + N_{RG})$ where N_R are number of molecules/complexes that only contain a red fluorophore and N_{GR} are the number of double-labeled molecules/complexes. The higher f_{G_T,R_T} and β are, the more the non-PIE red ACF will deviate from the true value. Nevertheless, when using PIE-RICS, the crosstalk term β goes to 0 and the amplitude of the red reduces to:

$$G_{RR}(0,0) = \frac{1}{N_{R_T}} \tag{22}$$

When PIE is not used, the cross-correlation is calculated between the green channel F_{GG} and the combined red channel F_{GR+RR}. The ccRICS amplitude is given by:

$$G_{GG\times(GR+RR)}(0,0) = \frac{\beta N_G + (\beta+1)N_{GR}}{N_{G_T}(N_{R_T} + \beta N_{G_T})} \tag{23}$$

with N_{G_T} being the total number of green labeled molecules and N_G the total number of molecules/complexes that contain only the green fluorophore. Even in the absence of truly correlating molecules ($N_{GR} = 0$), the amplitude of ccRICS will not be 0. However, when PIE is applied, the crosstalk parameter β is eliminated and the $ccRICS_{PIE}$ amplitude is again defined by:

$$G_{GG\times RR}(0,0) = \frac{N_{GR}}{N_{G_T}N_{R_T}} \tag{24}$$

Overall, dual color PIE-ccRICS is a crosstalk-free and robust approach to evaluate co-diffusion and interactions between different labeled molecules in a quantitative manner. Crosstalk free PIE-ccRICS was used to investigate the oligomerization status of the structural HIV-1 polyprotein Gag [23]. HeLa cells were transfected with mCherry- and mVenus-labeled Gag and the amount of cross correlation was quantified (Fig. 10C-F). A mobile and immobile fraction were observed with RICS. The results showed that the cross-correlating species are part of the immobile fraction, meaning that Gag-Gag interaction generate large and slow oligomers that cannot be resolved on the RICS timescale (and were further evaluated with TICS).

6.2. Raster lifetime image correlation spectroscopy

An additional advantage of using PIE-RICS is that the fluorescence lifetime information is stored in the photon arrival time and can be used

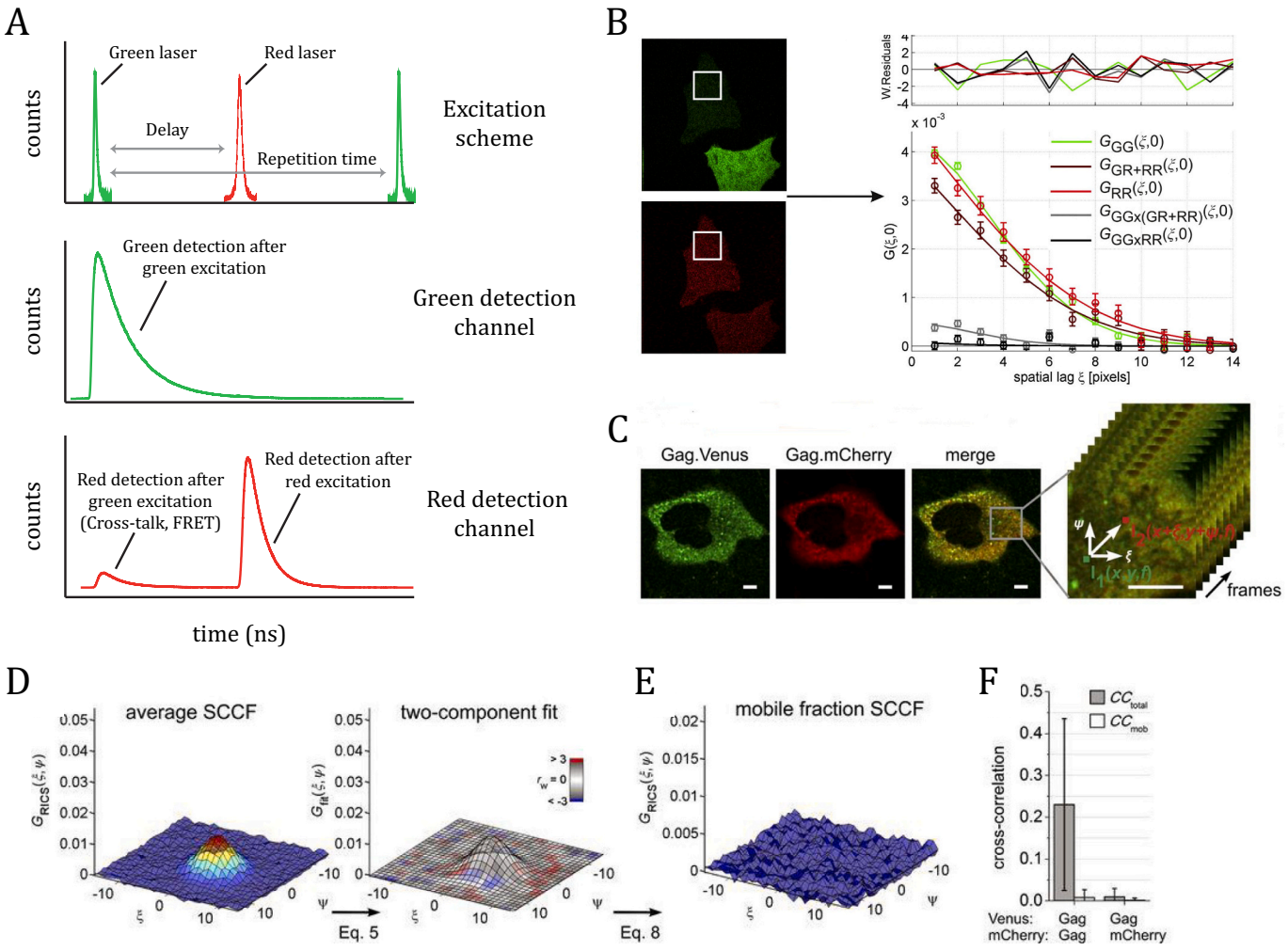

Fig. 10. Reducing spectral cross talk by combining RICS with PIE. A) Schematic of the dual-color PIE principle. In a typical PIE excitation scheme, the green and red lasers are pulsed at a given repetition rate and the red pulse is delayed with respect to the green one. The fluorescence emitted from the green fluorophore after green excitation is collected in the green detection channel. Thanks to the precise synchronization of excitation and detection, it is possible to distinguish in the red channel, and temporally separate, the fluorescence emitted by the red fluorophore after green excitation (caused by crosstalk or FRET) or after red excitation. B) Dual-color PIE-RICS in the cytosol of HeLa cells expressing eGFP (green) and mCherry (red). Reprinted from Biophysical Journal, Vol 105, Issue 4, /edition number, Jelle Hendrix, Waldemar Schrimpf, Matthias Höller, Don C. Lamb, Pulsed Interleaved Excitation Fluctuation Imaging, Pages 848–861, Fig. 2B-C, Copyright (2013), with permission from Elsevier [63]. Representative confocal images are shown on the left side with the white square indicating the region where PIE-RICS measurements were performed. On the right side, the spatial auto- and cross-correlation functions are shown. G_{GG} = SACF of the green channel. G_{GR+RR} = SACF of the red channel. G_{RR} = SACF of red detection after red excitation, i.e. excluding the crosstalk contribution. $G_{GG\times(GR+RR)}$ = spatial CCF including crosstalk. $G_{GG\times RR}$ = SCCF excluding the crosstalk contribution. (C-F) Diffusion of HIV-1 Gag polyprotein analyzed by PIE-RICS. Reproduced from [23] under the terms of the Creative Common Attribution-Noncommercial-Share Alike 3.0 Unported Int. (CC BY-NC-SA 3.0) License https://creativecommons.org/licenses/by-nc-sa/3.0/). C) Representative confocal images of HeLa cells expressing Gag labeled with Venus or mCherry. CcRICS is performed on the ROI marked in gray, after acquiring several frames. The scale bar is 5 μm. D) CcRICS analyses of the cell shown in (C). The experimental SCCF is shown on the left and its two-component fit is shown on the right, color coded according to the weighted residuals parameter r_w (inset). E) SCCF of the mobile fraction, obtained by subtracting the static component. After subtracting the immobile fraction, there is no detectable cross-correlation, indicating that the Gag-Venus and Gag-mCherry molecules that interact with each other form complexes that are part of the immobile fraction F) Comparison of total cross-correlation (CC_{total}) and cross-correlation of the mobile fraction (CC_{mob}) for cells expressing Gag-Venus and Gag-mCherry versus cells expressing Gag-Venus and freely diffusing mCherry. This results further confirm that the cross-correlation between Gag molecules occurs in the immobile fraction. (For interpretation of the references to color in this figure legend, the reader is referred to the web version of this article.)

to correlate different species with a lifetime weighting approach. Similarly to fluorescence lifetime correlation spectroscopy (FLCS) [96–98], raster lifetime ICS (RLICS) can be performed by calculating lifetime filters for each species of interest and used to weight each photon in the PIE-RICS image [63] (Fig. 11). With this approach, crosstalk-free ccRICS can also be performed and, if the lifetime filters are substantially different, even species with the same spectra can be separated. In addition, RLICS can be used in single-color experiments to filter out background noise, such as Raman scattering, laser reflections and detector afterpulsing, which, especially at low concentrations, can distort the correlation function. RLICS improves the sensitivity of RICS from the nanomolar to the picomolar regime. RLICS is conceptually similar to FLCS, which has been exploited to investigate different biological phenomena. For instance, the Keyes group utilized FLCS to investigate the effect of a polymer, such as PEG, on a lipid bilayer. Their studies revealed that PEG not only dramatically increases the fluidity of lipid bilayer but also generates a discontinuous hydrophilic mesh within the membranes [99,100]. FLCS can also be applied in live cells, as shown by Chen and Irudayaraj, who used FLCS to investigate the binding of the epidermal growth factor receptor (EGFR) and its antagonist antibody in HEK293 cells [101].

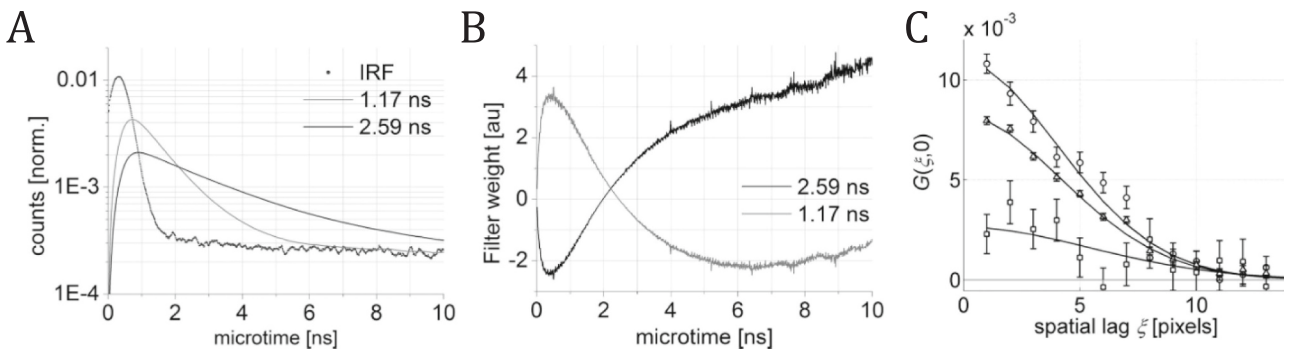

Fig. 11. RLICS method to discriminate species with the same spectra based on their different lifetime. Reprinted from Biophysical Journal, Vol 105, Issue 4, Jelle Hendrix, Waldemar Schrimpf, Matthias Höller, Don C. Lamb, Pulsed Interleaved Excitation Fluctuation Imaging, Pages 848–861, Fig. 5D-F, Copyright (2013), with permission from Elsevier [63]. A) Calculated fluorescence decay of free eGFP (2.59 ns) and quenched eGFP, part of an eGFP-mCherry tandem protein, (1.17 ns), convoluted with the instrument response function (IRF). B) Lifetime weighted filters calculated from the microtimes in (A). C) 1D SCCFs obtained using the RLICS analyses of live cells expressing an eGFP-mCherry tandem. Unfiltered (triangles), quenched-species filtered (circles), and non-quenched species filtered (squares) $G_{GG\times RR}(\xi,0)$ are shown. When filtered for the non-quenched species, i.e. freely diffusing eGFP, the cross-correlation is strongly reduced, as only the eGFP-mCherry tandem species should cross-correlate.

6.3. *Spectral RICS*

In an analogous way to RLICS, fluorophores with overlapping yet different emission spectra can be separated by calculating statistical filters based on the spectral information instead of the fluorescence lifetime. This method was originally developed for FCS [102] and later applied to spatial correlation using the raster spectral image correlation spectroscopy (RSICS) technique [91]. RSICS can be performed without TCSPC hardware, but different spectral regions need to be detected. This can be elegantly done using spectral detection where the spectral information is divided into several spectral regions (e.g. 32 spectral bins with the Zeiss commercial setup LSM 980). The result of a raster-scanned image with spectral detection is a stack in which every slice of the stack is the same ROI detected at a different wavelength and represents a spectral bin (Fig. 12A). If multiple frames are acquired, each frame consists in a hyperspectral stack. The spectral filters, determined using spectral images of the pure species (Fig. 12B, E), are then multiplied by each slice of the experimental stack, generating a spectrally weighted image. The spatial correlations can then be calculated on the newly generated weighted images and the contribution of crosstalk to the cross-correlation is eliminated (Fig. 12F). With spectral imaging, even very small differences in the emission spectra are enough to distinguish two species. For example, Atto488 and eGFP, which possess highly overlapping emission spectra, can be easily resolved. When these two species are free in solution, the RSICS calculated cross-correlation is zero [91]. However, this sensitivity is a double-edged sword in that precise filters are required. Hence, it is recommended to measure the filters of the pure species in as similar of an environment as possible to the true measurement.

Overall, RSICS is a powerful method that can be used both *in vitro* and in living cells to distinguish and correlate up to four fluorophores [24], without restricting the choice of labels according to ther separation of their excitation spectra. Dunsing and colleagues additionally implemented three-color RSICS to characterize the influenza A virus ternary polymerase complex (PC) in living cells (Fig. 12G-I). The three subunits of the complex; the polymerase acid protein (PA), the polymerase basic protein 1 (PB1) and polymerase basic protein 2 (PB2), were labeled with mEYFP, mEGFP and mCherry2, respectively [24]. To determine the stoichiometry of the complex, the diffusion coefficient and the brightness of each interaction partner were determined as well as the cross-correlation amplitudes between all the two-by-two combinations (Fig. 12H-I). The results suggested that each subunit is present as a dimer in the complex with PB1 and that PB1 is essential for complex formation. To further confirm that each subunit is present in the complex, Dunsing and colleagues extended the use of three-color RSICS data and developed a triple raster image correlation spectroscopy (TRICS) analysis, an approach similar to triple-correlation spectroscopy [103]. A 2:2:2 stoichiometry was determined by quantifying the relative triple-correlation, i.e., the ratio between the triple-correlation and ACFs amplitude, and it was estimated that, when all the subunits are present, 90 % of them contribute to ternary complex formation.

7. Conclusion

Over the past two decades, RICS has emerged as a very versatile technique to investigate molecular dynamics of biomolecules such as diffusion or aggregation. RICS combines the high time resolution of FCS with the spatial resolution of ICS, creating a method that can obtain spatially resolved dynamic information on the microsecond to second timescale. RICS is based on raster-scanning confocal microscopy and can be performed with either analog or single-photon-counting detectors. The popularity of this technique can be attributed to its easy of implementation. Indeed, this type of microscopy, combined with easier access to analyses software, is nowadays present in many life-science research labs.

Being an image-based analysis, RICS offers several advantages that make it particularly suitable for live-cell imaging experiments. First, it allows one to probe diffusion in different cellular compartments at the same time, and to build high resolution diffusion maps. In addition, acquiring information from an image instead of a single point helps mitigate the effect of local heterogeneities. The sensitivity of fluorescence fluctuation methods in general, and RICS in particular, to these heterogeneities have made their proper application often challenging. However, these heterogeneities can now be accounted for and corrected by simple detrending methods such as the subtraction of a moving average and/or intensity thresholding. Probing a larger area also helps reduce the effect of photobleaching and phototoxicity compared to single-point FCS. The timescales measurable with RICS makes it the technique of choice to investigate the diffusion of biomolecules in the cytosol. However, to evaluate the diffusion of very slow molecules, such as membrane proteins, TICS remains a more appropriate approach. Conversely, FCS is more suitable for investigating fast molecular processes, such as rotation.

Since its development, many efforts have been done to improve and extend the RICS method. For example, the spatial resolution of the diffusion maps generated by RICS analyses has been progressively enhanced. ARICS introduced the possibility of generating non-squared ROIs, which expanded the pool of analyzable cellular compartments and maximizes the data that can be included in the analysis. RICS has also been combined with the phasor analysis and with STED microscopy,

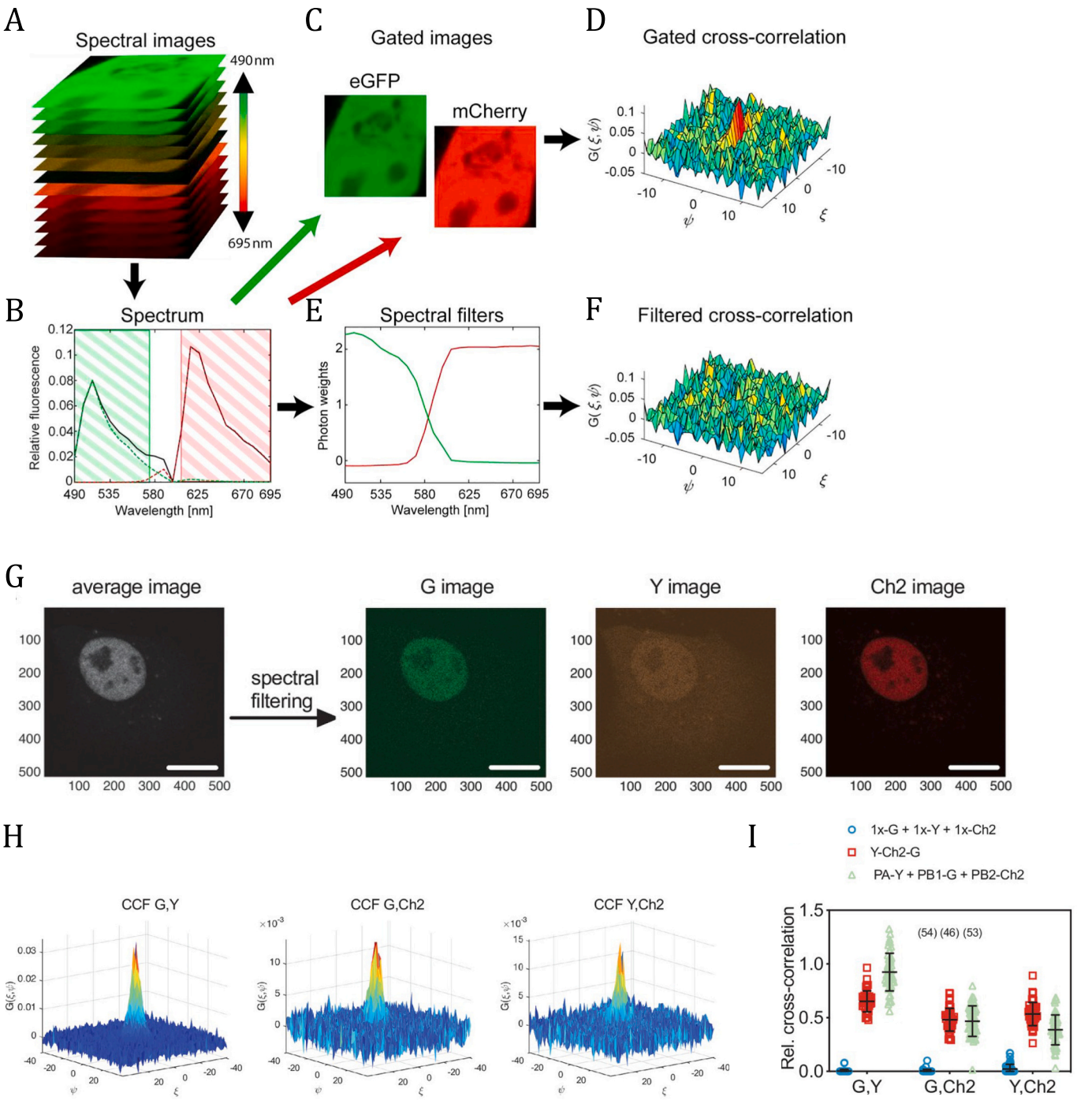

Fig. 12. Principle of spectral RICS and its application to study protein oligomerization in the influenza A virus. (A-F) Spectral RICS (RSICS) schematic. Reprinted from Methods (Elsevier), Vol 140, Waldemar Schrimpf, Veerle Lemmens, Nick Smisdom, Marcel Ameloot, Don C. Lamb, Jelle Hendrix, Crosstalk-free multicolor RICS using spectral weighting, Pages 97–111, Copyright (2018), with permission from Elsevier [91]. A) Acquisition of a spectrally resolved image stack, with spectral bins ranging from 490 to 695 nm. B) Emission spectra of eGFP (green dashed line), mCherry (red dashed line) and of a mixture of both (black solid line). The spectral ranges of eGFP and mCherry used in a channel-based analysis are highlighted as the hatched areas in green and red, respectively. C) For gated-RICS analyses, the spectral ranges of eGFP and mCherry defined in (B) are pooled and D) correlated, resulting in a residual cross-correlation. E) Spectral weights calculated from (B) in order to perform spectral RICS. The filters are applied to the image stack (A) before calculating the correlation functions. F) The resulting filtered cross-correlation function, which shows no residual CCF amplitude. (G-J) Three species RSICS measurements of the polymerase complex (PC) of influenza A virus (IAV) in the nucleus of A549 cells, adapted and reproduced from [24], Fig. 6A, C-D, under the terms of the Creative Common Attribution 4.0 Int. (CC-BY 4.0) License (https://creativecommons.org/licenses/by/4.0/). G) Representative fluorescence image (left) of A549 cells expressing IAV PC proteins tagged with fluorescence proteins as follows: PA-mEYFP, PB1-mEGFP and PB2-mCherry2. After applying the spectral filters, the image was decomposed into one image per channel, denoted as "Y", "G" and "Ch2", respectively. The scale bars are 10 μm. H) Representative RSICS cross-correlation functions obtained from the experiment outlined in (G). I) Relative cross-correlation values obtained from three-species RSICS measurement in cells co-expressing either freely diffusing mEGFP, mEYFP, and mCherry2 (blue, negative control of cross-correlation), or PA-mEYFP, PB1-mEGFP, PB2-mCherry2 (green) or mEYFP-mCherry2-mEGFP heterotrimers (red, positive control of cross-correlation). (For interpretation of the references to color in this figure legend, the reader is referred to the web version of this article.)

making it possible to obtain sub-micrometer spatial resolution. Dual-color RICS was then expanded to cross-correlation RICS, making this technique popular to investigate not only diffusion but also molecular interactions between two, fluorescently-labeled molecules. Using two channels, however, entails the need of correcting or minimizing spectral crosstalk. To this end, RICS was combined with pulsed interleaved excitation (PIE-RICS) to make use of the lifetime information (e.g. RLICS) and has recently been combined with spectral information in spectral RICS.

Overall, RICS and its technical advancements represent a powerful biophysical toolkit to precisely and reliably study the dynamic behavior of molecules in both space and time. The scanning aspect of RICS makes it well suited for measuring in live cells and tissue. The future of RICS looks very bright with many advances being made in fluorescence microscopy. Significant improvements are being made with respect to the fluorophores used with better photostability or novel photophysical properties. This is true for both synthetic dyes [104,105] as well as fluorescent proteins [106,107]. Also the analysis methods are continuing to advance making it possible to analyze the data more quickly and/or extract more information from the data. Recent examples include higher-order correlation analyses [108,109], which allow more species to be quantified from the data [108,109] and machine-learning methods, which may replace the correlation analysis altogether as has already been implemented for imaging FCS [110]. Although we have focused on RICS in this review, there are a myriad of related fluorescence fluctuation techniques that are also developing at a rapid pace including the entire family of ICS methods, 1D and 2D pair-correlation FCS [111], line [11,112] and circle scanning FCS [113] just to name a few. Taken together, we expect the application of fluctuation methods in general and RICS in particular to continue to grow and diversify into all branches of the biological, biophysical and biomedical sciences.

CRediT authorship contribution statement

Irene Gialdini: Writing – review & editing, Writing – original draft. **Jelle Hendrix:** Writing – review & editing, Conceptualization. **Don C. Lamb:** Writing – review & editing, Supervision, Conceptualization.

Declaration of competing interest

The authors declare the following financial interests/personal relationships which may be considered as potential competing interests:

Don C. Lamb and Jelle Hendrix have a patent, #WO2019/138028 issued to World Intellectual Property Organization, with respect to spectral RICS. The remaining author, Irene Gialdini, declares no known competing financial interests or personal relationships that could have appeared to influence the work reported in this paper.

Acknowledgements

We thank Paul Wiseman for scientific discussion. We thankfully acknowledge the financial support of the Deutsche Forschungsgemeinschaft (DFG, German Research Foundation) – Project-ID 201269156 – SFB 1032 Project B03 (to D.C.L.) and from the Federal Ministry of Education and Research (BMBF) and the Free State of Bavaria under the Excellence Strategy of the Federal Government and the Länder through the ONE MUNICH Project Munich Multiscale Biofabrication. D.C.L. gratefully acknowledges the financial support of the Ludwig-Maximilians-Universität München via, the Center for Nano-Science (CeNS) and the LMUinnovativ program BioImaging Network (BIN). J.H. acknowledges the Research Foundation Flanders (FWO, grant numbers G0H3716N, G0A8L24N, I000123N).

Data availability

We have included real data for illustration purposes. Data are available upon request.

References

[1] D. Magde, E. Elson, W.W. Webb, Thermodynamic fluctuations in a reacting system—measurement by fluorescence correlation spectroscopy, Phys. Rev. Lett. 29 (1972) 705–708.
[2] E.L. Elson, D. Magde, Fluorescence correlation spectroscopy. I. Conceptual basis and theory, Biopolymers 13 (2004) 1–27.
[3] D. Magde, E.L. Elson, W.W. Webb, Fluorescence correlation spectroscopy. II. An experimental realization, Biopolymers 13 (1974) 29–61.
[4] R. Rigler, Ü. Mets, J. Widengren, P. Kask, Fluorescence correlation spectroscopy with high count rate and low background: analysis of translational diffusion, Eur. Biophys. J. 22 (1993) 169–175.
[5] R.K.S. Felekyan, V. Kudryavtsev, C. Sandhagen, W. Becker, C.A.M. Seidel, Full Correlation from Picoseconds to Seconds by Time-Resolved and Time-Correlated Single Photon Detection, 2005.
[6] S.H.M. Weissman, G. Feher, Determination of molecular weights by fluctuation spectroscopy: application to DNA, Proc. Natl. Acad. Sci. USA 73 (1976) 2776–2780.
[7] N.O. Petersen, Scanning fluorescence correlation spectroscopy. I. Theory and simulation of aggregation measurements, Biophys. J. 49 (1986) 809–815.
[8] S.H.T. Meyer, Particle counting by fluorescence correlation spectroscopy. Simultaneous measurement of aggregation and diffusion of molecules in solutions and in membranes, Biophys. J. 54 (1988) 983–993.
[9] Q. Ruan, M.A. Cheng, M. Levi, E. Gratton, W.W. Mantulin, Spatial-temporal studies of membrane dynamics: scanning fluorescence correlation spectroscopy (SFCS), Biophys. J. 87 (2004) 1260–1267.
[10] K.M. Berland, P.T.C. So, Y. Chen, W.W. Mantulin, E. Gratton, Scanning two-photon fluctuation correlation spectroscopy: particle counting measurements for detection of molecular aggregation, Biophys. J. 71 (1996) 410–420.
[11] J. Ries, S. Chiantia, P. Schwille, Accurate determination of membrane dynamics with line-scan FCS, Biophys. J. 96 (2009) 1999–2008.
[12] J. Ries, P. Schwille, Studying slow membrane dynamics with continuous wave scanning fluorescence correlation spectroscopy, Biophys. J. 91 (2006) 1915–1924.
[13] J. Ries, P. Schwille, New concepts for fluorescence correlation spectroscopy on membranes, Phys. Chem. Chem. Phys. 10 (2008) 3487–3497.
[14] N.O. Petersen, D.C. Johnson, M.J. Schlesinger, Scanning fluorescence correlation spectroscopy. II. Application to virus glycoprotein aggregation, Biophys. J. 49 (1986) 817–820.
[15] N.O. Petersen, P.L. Hoddelius, P.W. Wiseman, O. Seger, K.E. Magnusson, Quantitation of membrane receptor distributions by image correlation spectroscopy: concept and application, Biophys. J. 65 (1993) 1135–1146.
[16] P.W. Wiseman, J.A. Squier, M.H. Ellisman, K.R. Wilson, Two-photon image correlation spectroscopy and image cross-correlation spectroscopy, J. Microsc. 200 (2000) 14–25.
[17] M.A. Digman, C.M. Brown, P. Sengupta, P.W. Wiseman, A.R. Horwitz, E. Gratton, Measuring fast dynamics in solutions and cells with a laser scanning microscope, Biophys. J. 89 (2005) 1317–1327.
[18] M.A. Digman, P. Sengupta, P.W. Wiseman, C.M. Brown, A.R. Horwitz, E. Gratton, Fluctuation correlation spectroscopy with a laser-scanning microscope: exploiting the hidden time structure, Biophys. J. 88 (2005) L33–L36.
[19] M.A. Digman, E. Gratton, Analysis of diffusion and binding in cells using the RICS approach, Microsc. Res. Tech. 72 (2009) 323–332.
[20] N.M. Clark, E. Hinde, C.M. Winter, A.P. Fisher, G. Crosti, I. Blilou, E. Gratton, P. N. Benfey, R. Sozzani, Tracking transcription factor mobility and interaction in Arabidopsis roots with fluorescence correlation spectroscopy, Elife 5 (2016).
[21] S.C. Norris, J. Humpolickova, E. Amler, M. Huranova, M. Buzgo, R. Machan, D. Lukas, M. Hof, Raster image correlation spectroscopy as a novel tool to study interactions of macromolecules with nanofiber scaffolds, Acta Biomater. 7 (2011) 4195–4203.
[22] M. Kluba, Y. Engelborghs, J. Hofkens, H. Mizuno, Inhibition of receptor dimerization as a novel negative feedback mechanism of EGFR signaling, PLoS One 10 (2015) e0139971.
[23] J. Hendrix, V. Baumgartel, W. Schrimpf, S. Ivanchenko, M.A. Digman, E. Gratton, H.G. Krausslich, B. Muller, D.C. Lamb, Live-cell observation of cytosolic HIV-1 assembly onset reveals RNA-interacting Gag oligomers, J. Cell Biol. 210 (2015) 629–646.
[24] V. Dunsing, A. Petrich, S. Chiantia, Multicolor fluorescence fluctuation spectroscopy in living cells via spectral detection, Elife 10 (2021) e69687.
[25] J. Lou, Q. Deng, X. Zhang, C.C. Bell, A.B. Das, N.G. Bediaga, C.O. Zlatic, T. M. Johanson, R.S. Allan, M.D.W. Griffin, P. Paradkar, K.F. Harvey, M.A. Dawson, E. Hinde, Heterochromatin protein 1 alpha (HP1alpha) undergoes a monomer to dimer transition that opens and compacts live cell genome architecture, Nucleic Acids Res. 52 (2024) 10918–10933.
[26] S. Anselmo, G. Sancataldo, V. Fodera, V. Vetri, Alpha-casein micelles-membranes interaction: flower-like lipid protein coaggregates formation, Biochim. Biophys. Acta Gen. Subj. 1866 (2022) 130196.
[27] A. Sasaki, J. Yamamoto, T. Jin, M. Kinjo, Raster image cross-correlation analysis for spatiotemporal visualization of intracellular degradation activities against exogenous DNAs, Sci. Rep. 5 (2015) 14428.
[28] J. Hnilicova, S. Hozeifi, E. Stejskalova, E. Duskova, I. Poser, J. Humpolickova, M. Hof, D. Stanek, The C-terminal domain of Brd2 is important for chromatin

interaction and regulation of transcription and alternative splicing, Mol. Biol. Cell 24 (2013) 3557–3568.
[29] Y. Thattikota, S. Tollis, R. Palou, J. Vinet, M. Tyers, D. D'Amours, Cdc48/VCP promotes chromosome morphogenesis by releasing condensin from self-entrapment in chromatin, Mol. Cell 69 (2018) 664–676, e665.
[30] S. Makaremi, M. Rose, S. Ranjit, M.A. Digman, D.M.E. Bowdish, J.M. Moran-Mirabal, Lateral diffusion of CD14 and TLR2 in macrophage plasma membrane assessed by raster image correlation spectroscopy and single particle tracking, Sci. Rep. 10 (2020) 19375.
[31] W. Schrimpf, A. Barth, J. Hendrix, D.C. Lamb, PAM: a framework for integrated analysis of imaging, single-molecule, and ensemble fluorescence data, Biophys. J. 114 (2018) 1518–1528.
[32] S. Ivanchenko, D.C. Lamb, Fluorescence correlation spectroscopy: principles and developments, in: Supramolecular Structure and Function 10, 2011, pp. 1–30.
[33] N.L. Thompson, Fluorescence correlation spectroscopy, in: J.R. Lakowicz (Ed.), Topics in Fluorescence Spectroscopy, Volume 1: Techniques vol. 1, Plenum Press, New York, 1991, pp. 337–378.
[34] S. Myong, S. Cui, P.V. Cornish, M.U. Gack, J.U. Jung, K.P. Hopfner, H. Taekjip, Cytosolic viral sensor RIG-I is a 5′-triphosphate–dependent translocase on double-stranded RNA, Science 323 (2009) 1070–1074.
[35] E. Ploetz, B. Ambrose, A. Barth, R. Borner, F. Erichson, A.N. Kapanidis, H.D. Kim, M. Levitus, T.M. Lohman, A. Mazumder, D.S. Rueda, F.D. Steffen, T. Cordes, S. W. Magennis, E. Lerner, A new twist on PIFE: photoisomerisation-related fluorescence enhancement, Methods Appl. Fluoresc. 12 (2023).
[36] A. Pannek, F.J. Houghton, A.M. Verhagen, S.K. Dower, E. Hinde, P.A. Gleeson, Dynamics of intracellular neonatal Fc receptor-ligand interactions in primary macrophages using biophysical fluorescence techniques, Mol. Biol. Cell 33 (2022) ar6.
[37] M. Longfils, N. Smisdom, M. Ameloot, M. Rudemo, V. Lemmens, G.S. Fernandez, M. Roding, N. Loren, J. Hendrix, A. Sarkka, Raster image correlation spectroscopy performance evaluation, Biophys. J. 117 (2019) 1900–1914.
[38] C.M. Brown, R.B. Dalal, B. Hebert, M.A. Digman, A.R. Horwitz, E. Gratton, Raster image correlation spectroscopy (RICS) for measuring fast protein dynamics and concentrations with a commercial laser scanning confocal microscope, J. Microsc. 229 (2008) 78–91.
[39] M.J. Rossow, J.M. Sasaki, M.A. Digman, E. Gratton, Raster image correlation spectroscopy in live cells, Nat. Protoc. 5 (2010) 1761–1774.
[40] J. Hendrix, T. Dekens, W. Schrimpf, D.C. Lamb, Arbitrary-region raster image correlation spectroscopy, Biophys. J. 111 (2016) 1785–1796.
[41] R. De Mets, A. Delon, M. Balland, O. Destaing, I. Wang, Dynamic range and background filtering in raster image correlation spectroscopy, J. Microsc. 279 (2020) 123–138.
[42] F. Acerbi, M. Perenzoni, High sensitivity photodetector for photon-counting applications, in: Photon Counting - Fundamentals and Applications, 2018.
[43] Hamamatsu-Photonics, Photomultiplier Tubes—Basics and Applications, Fourth edition, 2017.
[44] E. Gielen, N. Smisdom, M. VandeVen, B. De Clercq, E. Gratton, M. Digman, J. M. Rigo, J. Hofkens, Y. Engelborghs, M. Ameloot, Measuring diffusion of lipid-like probes in artificial and natural membranes by raster image correlation spectroscopy (RICS): use of a commercial laser-scanning microscope with analog detection, Langmuir 25 (2009) 5209–5218.
[45] P.D. Moens, E. Gratton, I.L. Salvemini, Fluorescence correlation spectroscopy, raster image correlation spectroscopy, and number and brightness on a commercial confocal laser scanning microscope with analog detectors (Nikon C1), Microsc. Res. Tech. 74 (2011) 377–388.
[46] M.A. Digman, P.W. Wiseman, A.R. Horwitz, E. Gratton, Detecting protein complexes in living cells from laser scanning confocal image sequences by the cross correlation raster image spectroscopy method, Biophys. J. 96 (2009) 707–716.
[47] E. Dobrinskikh, L. Lanzano, J. Rachelson, D. Cranston, R. Moldovan, T. Lei, E. Gratton, R.B. Doctor, Shank2 contributes to the apical retention and intracellular redistribution of NaPiIIa in OK cells, Am. J. Phys. Cell Phys. 304 (2013) C561–C573.
[48] P. Schwille, F. Meyer-Almes, R. Rigler, Dual-color fluorescence cross-correlation spectroscopy for multicomponent diffusional analysis in solution, Biophys. J. 72 (1997) 1878–1886.
[49] S.A. Kim, K.G. Heinze, K. Bacia, M.N. Waxham, P. Schwille, Two-photon cross-correlation analysis of intracellular reactions with variable stoichiometry, Biophys. J. 88 (2005) 4319–4336.
[50] Y.H. Foo, N. Naredi-Rainer, D.C. Lamb, S. Ahmed, T. Wohland, Factors affecting the quantification of biomolecular interactions by fluorescence cross-correlation spectroscopy, Biophys. J. 102 (2012) 1174–1183.
[51] J.Y.H. Balakrishnan Kannan, Ping Liu, Ichiro Maruyama, Jeak Ling Ding, Thorsten Wohland, Electron multiplying charge-coupled device camera based fluorescence correlation spectroscopy, Anal. Chem. 78 (2006) 3444–3451.
[52] G.L.B. Kannan, T. Sudhaharan, S. Ahmed, I. Maruyama, T. Wohland, Spatially resolved total internal reflection fluorescence correlation microscopy using an electron multiplying charge-coupled device camera, Anal. Chem. 79 (2007) 4463–4470.
[53] N. Bag, J. Sankaran, A. Paul, R.S. Kraut, T. Wohland, Calibration and limits of camera-based fluorescence correlation spectroscopy: a supported lipid bilayer study, Chemphyschem 13 (2012) 2784–2794.
[54] D.J. Needleman, Y. Xu, T.J. Mitchison, Pin-hole array correlation imaging: highly parallel fluorescence correlation spectroscopy, Biophys. J. 96 (2009) 5050–5059.
[55] J. Brugues, D. Needleman, Physical basis of spindle self-organization, Proc. Natl. Acad. Sci. USA 111 (2014) 18496–18500.
[56] D. Oh, A. Zidovska, Y. Xu, D.J. Needleman, Development of time-integrated multipoint moment analysis for spatially resolved fluctuation spectroscopy with high time resolution, Biophys. J. 101 (2011) 1546–1554.
[57] M. Vitali, L. Terenius, F. Zappa, R. Rigler, D. Bronzi, A.J. Krmpot, S.N. Nikolic, F.-J. Schmitt, C. Junghans, S. Tisa, T. Friedrich, V. Vukojevic, A single-photon avalanche camera for fluorescence lifetime imaging microscopy and correlation spectroscopy, IEEE J. Sel. Top. Quantum Electron. 20 (2014) 344–353.
[58] A.J. Krmpot, S.N. Nikolic, S. Oasa, D.K. Papadopoulos, M. Vitali, M. Oura, S. Mikuni, P. Thyberg, S. Tisa, M. Kinjo, L. Nilsson, L. Terenius, R. Rigler, V. Vukojevic, Functional fluorescence microscopy imaging: quantitative scanning-free confocal fluorescence microscopy for the characterization of fast dynamic processes in live cells, Anal. Chem. 91 (2019) 11129–11137.
[59] S. Oasa, A.J. Krmpot, S.N. Nikolic, A.H.A. Clayton, I.F. Tsigelny, J.P. Changeux, L. Terenius, R. Rigler, V. Vukojevic, Dynamic cellular cartography: mapping the local determinants of oligodendrocyte transcription factor 2 (OLIG2) function in live cells using massively parallel fluorescence correlation spectroscopy integrated with fluorescence lifetime imaging microscopy (mpFCS/FLIM), Anal. Chem. 93 (2021) 12011–12021.
[60] S.N. Nikolic, S. Oasa, A.J. Krmpot, L. Terenius, M.R. Belic, R. Rigler, V. Vukojevic, Mapping the direction of nucleocytoplasmic transport of glucocorticoid receptor (GR) in live cells using two-foci cross-correlation in massively parallel fluorescence correlation spectroscopy (mpFCS), Anal. Chem. 95 (2023) 15171–15179.
[61] K.S.P. Schwille, S. Kummer, A.A. Heikal, W.E. Moerner, W.W. Webb, Fluorescence correlation spectroscopy reveals fastoptical excitation-driven intramolecular dynamicsof yellow fluorescent proteins, PNAS 97 (2000).
[62] R.M. Dickson, A.B. Cubitt, R.Y. Tsien, W.E. Moerner, On/off blinking and switching behaviour of single molecules of green fluorescent protein, Nature 388 (1997) 355–358.
[63] J. Hendrix, W. Schrimpf, M. Holler, D.C. Lamb, Pulsed interleaved excitation fluctuation imaging, Biophys. J. 105 (2013) 848–861.
[64] Y. Ohsugi, M. Kinjo, Multipoint fluorescence correlation spectroscopy with total internal reflection fluorescence microscope, J. Biomed. Opt. 14 (2009) 014030.
[65] S. Daetwyler, R.P. Fiolka, Light-sheets and smart microscopy, an exciting future is dawning, Commun. Biol. 6 (2023) 502.
[66] T. Wohland, X. Shi, Jagadish Sankaran, Ernst H.K. Stelzer, Single plane illumination fluorescence correlation spectroscopy (SPIM-FCS) probes inhomogeneous three-dimensional environments, Opt. Express 18 (2010) 10627–10641.
[67] J. Capoulade, M. Wachsmuth, L. Hufnagel, M. Knop, Quantitative fluorescence imaging of protein diffusion and interaction in living cells, Nat. Biotechnol. 29 (2011) 835–839.
[68] A.P. Singh, J.W. Krieger, J. Buchholz, E. Charbon, J. Langowski, T. Wohland, The performance of 2D array detectors for light sheet based fluorescence correlation spectroscopy, Opt. Express 21 (2013) 8652–8668.
[69] L. Scipioni, M. Di Bona, G. Vicidomini, A. Diaspro, L. Lanzano, Local raster image correlation spectroscopy generates high-resolution intracellular diffusion maps, Commun. Biol. 1 (2018) 10.
[70] P.N. Hedde, R.M. Dorlich, R. Blomley, D. Gradl, E. Oppong, A.C. Cato, G. U. Nienhaus, Stimulated emission depletion-based raster image correlation spectroscopy reveals biomolecular dynamics in live cells, Nat. Commun. 4 (2013) 2093.
[71] J. Brewer, M. Bloksgaard, J. Kubiak, J.A. Sorensen, L.A. Bagatolli, Spatially resolved two-color diffusion measurements in human skin applied to transdermal liposome penetration, J. Invest. Dermatol. 133 (2013) 1260–1268.
[72] M. Leutenegger, T. Lasser, E.K. Sinner, R. Robelek, Imaging of G protein-coupled receptors in solid-supported planar lipid membranes, Biointerphases 3 (2008) FA136.
[73] M. Guthmann, C. Qian, I. Gialdini, T. Nakatani, A. Ettinger, T. Schauer, I. Kukhtevich, R. Schneider, D.C. Lamb, A. Burton, M.E. Torres-Padilla, A change in biophysical properties accompanies heterochromatin formation in mouse embryos, Genes Dev. 37 (2023) 336–350.
[74] L. Scipioni, E. Gratton, A. Diaspro, L. Lanzano, Phasor analysis of local ICS detects heterogeneity in size and number of intracellular vesicles, Biophys. J. 111 (2016) 619–629.
[75] D.M. Jameson, E. Gratton, R.D. Hall, The measurement and analysis of heterogeneous emissions by multifrequency phase and modulation fluorometry, Appl. Spectrosc. Rev. 20 (1984) 55–106.
[76] A.H. Clayton, Q.S. Hanley, P.J. Verveer, Graphical representation and multicomponent analysis of single-frequency fluorescence lifetime imaging microscopy data, J. Microsc. 213 (2004) 1–5.
[77] G.I. Redford, R.M. Clegg, Polar plot representation for frequency-domain analysis of fluorescence lifetimes, J. Fluoresc. 15 (2005) 805–815.
[78] M.A. Digman, V.R. Caiolfa, M. Zamai, E. Gratton, The phasor approach to fluorescence lifetime imaging analysis, Biophys. J. 94 (2008) L14–L16.
[79] S.W. Hell, J. Wichmann, Breaking the diffraction resolution limit by stimulated emission: stimulated-emission-depletion fluorescence microscopy, Opt. Lett. 19 (1994) 780–782.
[80] S.W. Hell, T.A. Klar, Subdiffraction resolution in far-field fluorescence microscopy, Opt. Lett. 24 (1999).
[81] L. Kastrup, H. Blom, C. Eggeling, S.W. Hell, Fluorescence fluctuation spectroscopy in subdiffraction focal volumes, Phys. Rev. Lett. 94 (2005) 178104.
[82] B. Hein, K.I. Willig, H. SW, Stimulated emission depletion (STED) nanoscopy of afluorescent protein-labeled organelle inside aliving cell, Proc. Natl. Acad. Sci. USA 105 (2008) 14271–14276.

[83] A. Hense, B. Prunsche, P. Gao, Y. Ishitsuka, K. Nienhaus, G.U. Nienhaus, Monomeric Garnet, a far-red fluorescent protein for live-cell STED imaging, Sci. Rep. 5 (2015) 18006.
[84] G. Matela, P. Gao, G. Guigas, A.F. Eckert, K. Nienhaus, G.U. Nienhaus, A far-red emitting fluorescent marker protein, mGarnet2, for microscopy and STED nanoscopy, Chem. Commun. (Camb.) 53 (2017) 979–982.
[85] A. Stockhammer, F. Bottanelli, Appreciating the small things in life: STED microscopy in living cells, J. Phys. D. Appl. Phys. 54 (2021).
[86] M. Bernabé-Rubio, M. Bosch-Fortea, E. Garcia, J. Bernardino de la Serna, M. A. Alonso, Adaptive lipid immiscibility and membrane remodeling are active functional determinants of primary ciliogenesis, Small Methods 5 (2021) e2000711.
[87] F. Schneider, D. Waithe, M.P. Clausen, S. Galiani, T. Koller, G. Ozhan, C. Eggeling, E. Sezgin, Diffusion of lipids and GPI-anchored proteins in actin-free plasma membrane vesicles measured by STED-FCS, Mol. Biol. Cell 28 (2017) 1507–1518.
[88] V. Mueller, C. Ringemann, A. Honigmann, G. Schwarzmann, R. Medda, M. Leutenegger, S. Polyakova, V.N. Belov, S.W. Hell, C. Eggeling, STED nanoscopy reveals molecular details of cholesterol- and cytoskeleton-modulated lipid interactions in living cells, Biophys. J. 101 (2011) 1651–1660.
[89] M. Bernabé-Rubio, G. Andres, J. Casares-Arias, J. Fernandez-Barrera, L. Rangel, N. Reglero-Real, D.C. Gershlick, J.J. Fernandez, J. Millan, I. Correas, D.G. Miguez, M.A. Alonso, Novel role for the midbody in primary ciliogenesis by polarized epithelial cells, J. Cell Biol. 214 (2016) 259–273.
[90] B.K. Müller, E. Zaychikov, C. Brauchle, D.C. Lamb, Pulsed interleaved excitation, Biophys. J. 89 (2005) 3508–3522.
[91] W. Schrimpf, V. Lemmens, N. Smisdom, M. Ameloot, D.C. Lamb, J. Hendrix, Crosstalk-free multicolor RICS using spectral weighting, Methods 140-141 (2018) 97–111.
[92] A.N. Kapanidis, T.A. Laurence, N.K. Lee, E. Margeat, X. Kong, S. Weiss, Alternating-laser excitation of single molecules, Acc. Chem. Res. 38 (2005) 523–533.
[93] A.N. Kapanidis, N.K. Lee, T.A. Laurence, S. Doose, E. Margeat, S. Weiss, Fluorescence-aided molecule sorting: analysis of structure and interactions by alternating-laser excitation of single molecules, Proc. Natl. Acad. Sci. USA 101 (2004) 8936–8941.
[94] J. Hendrix, D.C. Lamb, Pulsed interleaved excitation: principles and applications, Methods Enzymol. 518 (2013) 205–243.
[95] J. Hendrix, D.C. Lamb, Implementation and application of pulsed interleaved excitation for dual-color FCS and RICS, Methods Mol. Biol. 1076 (2014) 653–682.
[96] M.W. Martin Böhmer, Hans-Jürgen Rahn, Rainer Erdmann, Jörg Enderlein, Time-resolved fluorescence correlation spectroscopy, Chem. Phys. Lett. 353 (2002).
[97] S. Felekyan, S. Kalinin, H. Sanabria, A. Valeri, C.A. Seidel, Filtered FCS: species auto- and cross-correlation functions highlight binding and dynamics in biomolecules, Chemphyschem 13 (2012) 1036–1053.
[98] P. Kapusta, M. Wahl, A. Benda, M. Hof, J. Enderlein, Fluorescence lifetime correlation spectroscopy, J. Fluoresc. 17 (2007) 43–48.
[99] H. Basit, S.G. Lopez, T.E. Keyes, Fluorescence correlation and lifetime correlation spectroscopy applied to the study of supported lipid bilayer models of the cell membrane, Methods 68 (2014) 286–299.
[100] T. Tabarin, A. Martin, R.J. Forster, T.E. Keyes, Poly-ethylene glycol induced super-diffusivity in lipid bilayer membranes, Soft Matter 8 (2012).
[101] J. Chen, J. Irudayaraj, Fluorescence lifetime cross correlation spectroscopy resolves EGFR and antagonist interaction in live cells, Anal. Chem. 82 (2010) 6415–6421.
[102] A. Benda, P. Kapusta, M. Hof, K. Gaus, Fluorescence spectral correlation spectroscopy (FSCS) for probes with highly overlapping emission spectra, Opt. Express 22 (2014) 2973–2988.
[103] W.K. Ridgeway, D.P. Millar, J.R. Williamson, Quantitation of ten 30S ribosomal assembly intermediates using fluorescence triple correlation spectroscopy, Proc. Natl. Acad. Sci. USA 109 (2012) 13614–13619.
[104] J. Bucevicius, R. Gerasimaite, K.A. Kiszka, S. Pradhan, G. Kostiuk, T. Koenen, G. Lukinavicius, A general highly efficient synthesis of biocompatible rhodamine dyes and probes for live-cell multicolor nanoscopy, Nat. Commun. 14 (2023) 1306.
[105] J.B. Grimm, A.N. Tkachuk, R. Patel, S.T. Hennigan, A. Gutu, P. Dong, V. Gandin, A.M. Osowski, K.L. Holland, Z.J. Liu, T.A. Brown, L.D. Lavis, Optimized red-absorbing dyes for imaging and sensing, J. Am. Chem. Soc. 145 (2023) 23000–23013.
[106] T.W.J. Gadella Jr., L. van Weeren, J. Stouthamer, M.A. Hink, A.H.G. Wolters, B.N. G. Giepmans, S. Aumonier, J. Dupuy, A. Royant, mScarlet3: a brilliant and fast-maturing red fluorescent protein, Nat. Methods 20 (2023) 541–545.
[107] M. Hirano, R. Ando, S. Shimozono, M. Sugiyama, N. Takeda, H. Kurokawa, R. Deguchi, K. Endo, K. Haga, R. Takai-Todaka, S. Inaura, Y. Matsumura, H. Hama, Y. Okada, T. Fujiwara, T. Morimoto, K. Katayama, A. Miyawaki, A highly photostable and bright green fluorescent protein, Nat. Biotechnol. 40 (2022) 1132–1142.
[108] F. Abdollah-Nia, M.P. Gelfand, A. Van Orden, Artifact-free and detection-profile-independent higher-order fluorescence correlation spectroscopy for microsecond-resolved kinetics. 1. Multidetector and sub-binning approach, J. Phys. Chem. B 121 (2017) 2373–2387.
[109] J.L. Mitchell, N.L. Thompson, High order autocorrelation in fluorescence correlation spectroscopy, in: R. Rigler, E.S. Elson (Eds.), Fluorescence Correlation Spectroscopy: Theory and Applications, Springer Berlin Heidelberg, Berlin, Heidelberg, 2001, pp. 438–458.
[110] W.H. Tang, S.R. Sim, D.Y.K. Aik, A.V.S. Nelanuthala, T. Athilingam, A. Rollin, T. Wohland, Deep learning reduces data requirements and allows real-time measurements in imaging FCS, Biophys. J. 123 (2024) 655–666.
[111] A. Solano, J. Lou, L. Scipioni, E. Gratton, E. Hinde, Radial pair correlation of molecular brightness fluctuations maps protein diffusion as a function of oligomeric state within live-cell nuclear architecture, Biophys. J. 121 (2022) 2152–2167.
[112] A.F. Eckert, P. Gao, J. Wesslowski, X. Wang, J. Rath, K. Nienhaus, G. Davidson, G. U. Nienhaus, Measuring ligand-cell surface receptor affinities with axial line-scanning fluorescence correlation spectroscopy, Elife 9 (2020).
[113] G. Gunther, D.M. Jameson, J. Aguilar, S.A. Sanchez, Scanning fluorescence correlation spectroscopy comes full circle, Methods 140-141 (2018) 52–61.